Vol. 4, 1, 3–61 (1997)

Archives of Computational Methods in Engineering
State of the art reviews

Finite Element Analysis of Shell Structures

M.L. Bucalem

Laboratório de Mecânica Computacional
Departamento de Engenharia de Estruturas e Fundações
Escola Politécnica da Universidade de São Paulo
05508-900 São Paulo, SP, Brasil

K.J. Bathe

Department of Mechanical Engineering
Massachusetts Institute of Technology
Cambridge, MA 02139, USA

Summary

A survey of effective finite element formulations for the analysis of shell structures is presented. First, the basic requirements for shell elements are discussed, in which it is emphasized that generality and reliability are most important items. A general displacement-based formulation is then briefly reviewed. This formulation is not effective, but it is used as a starting point for developing a general and effective approach using the mixed interpolation of the tensorial components. The formulation of various MITC elements (that is, elements based on **M**ixed **I**nterpolation of **T**ensorial **C**omponents) are presented. Theoretical results (applicable to plate analysis) and various numerical results of analyses of plates and shells are summarized. These illustrate some current capabilities and the potential for further finite element developments.

1. INTRODUCTION

There is no need to discuss the importance of shell structures. Their efficient load–carrying capabilities have rendered their use widespread in a variety of engineering applications [1]. The continuous development of new structural materials leads to ever increasingly complex structural designs that require careful analysis.

Although analytical techniques are very important, the use of numerical methods to solve shell mathematical models of complex structures has become an essential ingredient in the design process. The finite element method has been the fundamental numerical procedure for the analysis of shells.

Ideally, the structural designer or analyst should be able to concentrate on the mechanical behavior of the structure and pay close attention to the underlying design issues. The finite element procedure should be used merely as a tool to obtain the solution of the mathematical model chosen to describe the structure. Unfortunately, this is not what usually happens in shell finite element analysis. Frequently, the analyst is required to be an expert in shell element technology to use confidently his/her finite element results. This is mainly due to the proliferation of elements that do not always work *i.e.*, are not reliable. It is our view that the use of reliable finite elements should always be a requirement. Although this may seem a very basic condition, the literature gives many elements that perform effectively in some cases but fail severely in others. Nevertheless, their use with "care" is recommended.

An important consideration discussed in [2] is that shell finite elements are nowadays being integrated in CAD (Computer Aided Design) systems, exposing design engineers that are relatively inexperienced with the details of shell element technology to the use of such elements. In this setting, the recommendation that a particular element should be used with care is meaningless, and the reliability of the elements is a strict requirement. Also, in such an environment, shell elements that are only adequate for a certain class of problems *i.e.*,

 ISSN: 1134–3060 Received: September 1995

for thin shell situations or for specific shell geometries and/or loading conditions are not as suitable as general shell elements.

In order to exemplify the kind of engineering problems that we want to be able to solve confidently with shell finite element formulations, we selected the problems shown in Figures 1 and 2. These problems indicate the complexity of shell modeling that we are aiming for and point out that the final objective of our formulations is to be able to address practical and challenging *engineering* problems. In the later part of this work we present some sample solutions that are relatively simple problems when compared with the ones above mentioned. Nevertheless, those problems are carefully selected to display the elements' predictive capabilities and to assure reliability. Therefore, it is important to bear in mind that the sole purpose of solving the sample problems is to guarantee that we can actually solve confidently *engineering* problems.

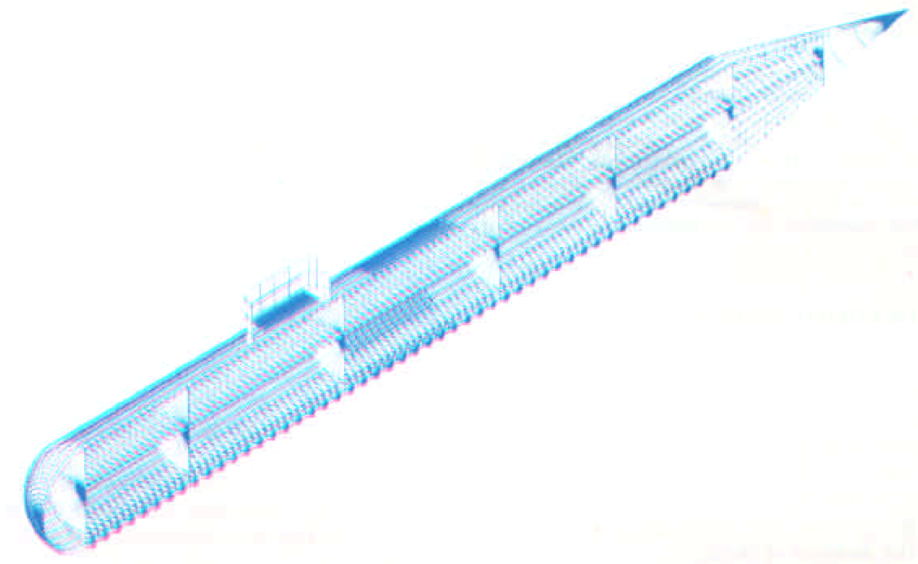

Figure 1. Model of a submarine hull on dock

The research activity in the area of finite elements for plate and shell structures spans a period of over three decades and continues to be very intense. Although we do not intent to present here a comprehensive review of what has been accomplished in shell element technology, we plan to briefly mention some key aspects of this research area before concentrating on the approach that we believe has produced so far the most efficient and reliable plate and shell elements.

The first step is to select an appropriate mathematical model. The thin shell theories that developed from the fundamental work of Love [3] and lead to the Koiter–Sanders theory [4, 5] have been used as mathematical models to propose shell elements. Also, a number of simplified thin shell theories that are derived by imposing restrictions either on the shell geometry or the loading conditions, or both, have been used to formulate shell elements. Many of such shell elements are discussed in [6] where a catalogue of elements is presented.

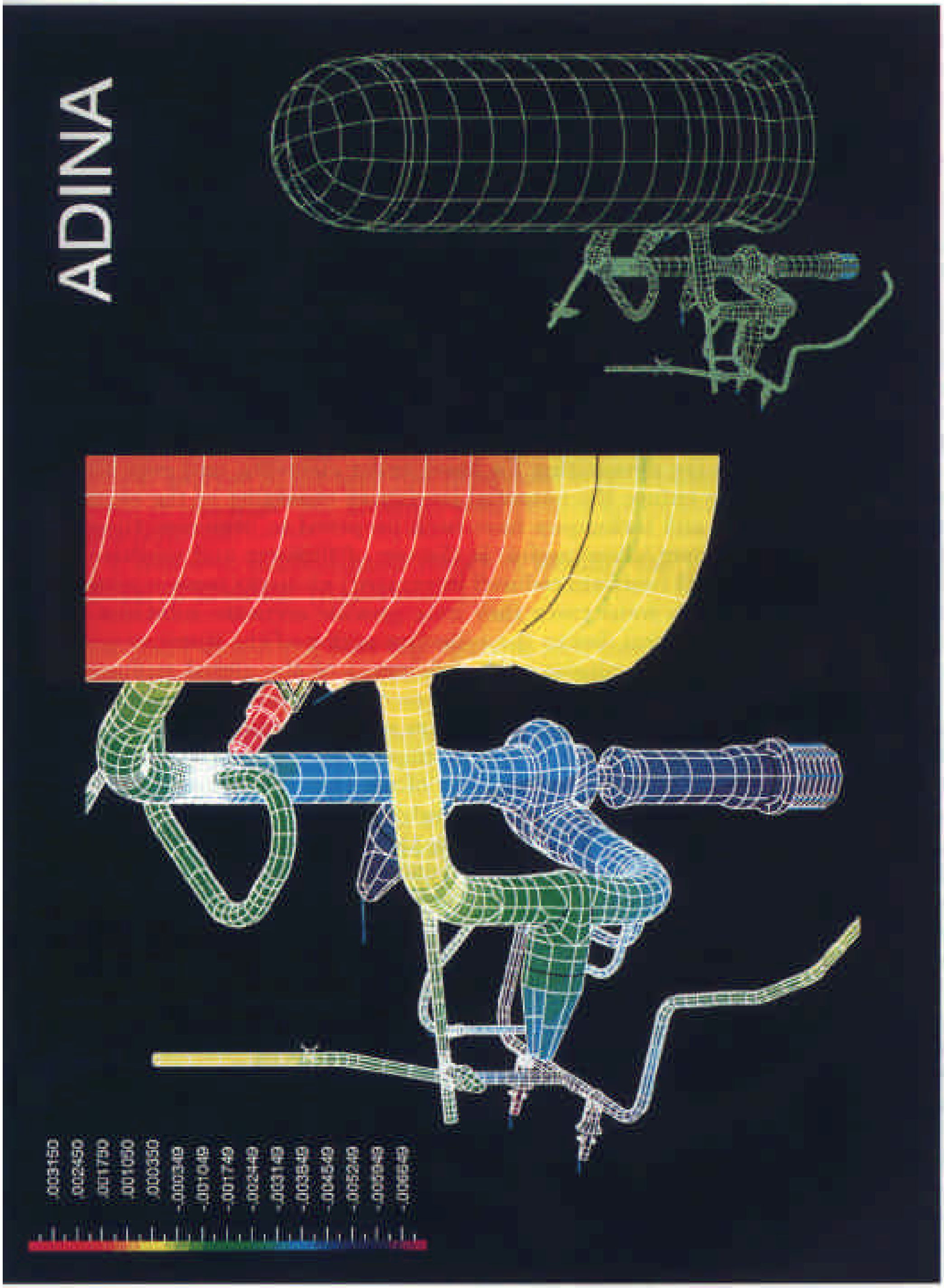

Figure 2. Model of a pressure vessel with piping

The approach of degenerating the shell from a solid is a very attractive alternative to the use of a thin shell theory. In this approach the shell behavior is described by imposing judiciously chosen kinematic and mechanical assumptions on the three–dimensional continuum mechanics conditions. The resulting theory corresponds for plate bending situations to the Reissner–Mindlin plate theory. This approach has been first presented, in the context of a shell element formulation by Ahmad *et. al.* [7] and has some key features that make it very suitable for shell finite element constructions, namely:

- The formulation is applicable to any shell geometry.
- The formulation is adequate for thin and thick situations.
- The formulation leads to C^0 conforming displacement-based elements.
- The formulation uses only engineering nodal point degrees of freedom such as displacements and rotations.

Shell elements based on this approach have been formulated for general nonlinear analysis (material and geometric nonlinear) by Ramm [8] and Bathe and Bolourchi [9].

Although the pure displacement-based formulation of these elements has all the above mentioned appealing features, which are very desirable if the elements are to be used in engineering practice, they do suffer from the serious deficiency of membrane and shear locking. The locking effects are devastating for lower–order elements, and even for higher–order elements they severely reduce the potential predictive capability of the elements.

A number of approaches and techniques have been proposed to overcome these difficulties. The simplest one, however unsuccessful, is the use of uniform and selective reduced integration. In general the URI (uniform reduced integrated) elements possess spurious zero energy modes, and although in some cases they may provide accurate solutions, in other cases a global mechanism may form due to the collective action of the spurious zero energy modes causing rank deficiency (or almost rank deficiency) of the global stiffness matrix. Even if a global mechanism does not arise, a near–mechanism might be activated which leads to unacceptable answers. The recommendation of disregarding solutions that have been affected by spurious energy modes is almost impossible to observe since, when the solution of the problem is not known, the judgment of whether a solution is “good” or not is very difficult to make. The SRI (selective reduced integrated) elements, although to a smaller degree, suffer from the same deficiencies as the URI elements and in some cases show very low convergence rates. Both types of elements are quite sensitive to geometric distortions. The above considerations make clear that the use of reduced integration is an unreliable technique to deal with locking effects. Nevertheless, the literature is rich in uniform and selective reduced integrated elements for plates and shells. We refer here just to the early works on reduced integration [10, 11, 12]. We note that in some cases it is possible to show a total equivalence between the use of reduced integration and a mixed formulation [13, 14]. In such an event reduced integration may be an efficient way of implementing a mixed method but the analysis of whether the formulation is a good formulation or not has to be made in the context of mixed methods.

Belytschko and co-workers developed the concept of spurious mode control [15, 16] in an attempt to use reduced integration and avoid the possibility of having spurious zero energy modes. Although successful in suppressing the spurious modes, their formulation is not transparent, requiring the use of some numerically adjusted factors.

It is our view that the development of shell finite elements should be guided by the following requirements:

1. The elements should be reliable
2. The elements should be computationally effective
3. The element formulation should be general *i.e.*, the elements should be applicable to:

– nonlinear analysis (geometric and material non-linear solutions),
– thick and thin plate/shell situations,
– any shell geometry

4. The formulation of the elements should be mechanistically clear and sufficiently simple to render the elements suitable for engineering analysis.

The continuum-based degenerated shell elements satisfy requirements 3 and 4, but the lower-order elements do not satisfy requirements 1 and 2, and the higher–order 16-node element does not sufficiently satisfy requirement 2, due to the effects of membrane and shear locking.

Ideally, considering requirements 1 and 2, the element formulation would lead to finite element discretizations that could be shown *mathematically* to be stable, convergent and to have optimal error bounds. In plate analysis much progress has been made in this regard. Especially, the MITC family of Reissner-Mindlin plate bending elements has been developed by Bathe *et.al.* and has a strong mathematical foundation that assures the convergence of the discretizations with optimal error bounds for the displacement variables. The theoretical foundations of the elements can be found in [17, 18, 19, 20] and additional theoretical and numerical results are presented in [21, 22, 23, 24, 25].

In general shell analysis, as stated in requirement 3, the situation is quite different. A mathematical analysis of the type just mentioned is not available. However, a very valuable contribution in this direction, although restricted in its applicability, has been published by Pitkäranta [26].

Since a complete mathematical theory is lacking, the following conditions should be strictly enforced to satisfy requirement 1:

a) The elements should not have any spurious zero energy mode.
b) The elements should not membrane or shear lock, when used in reasonably distorted meshes[1].
c) The predictive capability of the elements should be high and relatively insensitive to geometric distortions.

The conditions a) to c) represent a major difficulty in arriving at reliable shell elements. The conditions regarding locking and spurious energy modes are further discussed in Section 3.3. It is also well known that many shell elements perform well when of regular (say rectangular) shape but their predictive capabilities deteriorate rapidly as the elements are geometrically distorted. Since (in order to model a complex shell geometry) distorted elements are invariably employed in engineering practice, it is important to assure that element distortions do not lead to a significative loss in solution accuracy.

Of course, insight into element behavior and the use of numerical experiments are important in the design of elements that satisfy the above conditions. It is our view that an element which fails any one of these conditions should not be used in engineering practice.

The Mixed Interpolation of the Tensorial Components (MITC) approach has been used successfully to propose shell elements that satisfy the above conditions and requirement 2. Also, the formulation of the MITC elements preserves the essential and appealing characteristics of the continuum-based degenerated shell elements, therefore satisfying requirements 3 and 4.

The approach of mixed interpolation of tensorial components for shell elements finds its roots in the work of Dvorkin and Bathe [21], who developed a 4-node general shell element, called the MITC4 element. This element degenerates to the MITC4 plate bending element

[1] We shall in the following say that an element does not membrane or shear lock if such phenomena are not observed as long as the element is not severely distorted.

when the geometry is flat, the analysis is linear and the plate is subjected to transverse loading only, and then is closely related to the elements proposed by Hughes and Tezduyar [27] and MacNeal [28]. However, the MITC4 element was originally proposed for shell analysis and this is where assumed covariant strain component fields were first introduced. The subsequent developments undertaken with the MITC approach for general shell analysis are discussed in sections 3.3 and 4.

In the following sections we first discuss the continuum mechanics formulation of the displacement-based shell elements for general nonlinear analysis. This formulation is obtained in Section 2 by a consistent linearization of the principle of virtual work which contains the kinematic and stress assumptions of the three-dimensional large deformation behavior of a general shell. The resulting element formulation presented on Section 3 considers large displacements and rotations.

Since the pure displacement formulation even for higher-order elements do not fully satisfies the requirements that were outlined earlier, the formulation is extended in Section 4 to a mixed interpolation of strains and displacements to arrive at effective elements. In section 4.2 we summarize the mathematical theory of the MITC plate bending elements. This mathematical analysis besides providing a framework to construct optimally convergent plate bending elements, gives much insight into the shear locking phenomenon aiding, of course, the construction of new shear locking free shell elements. In any case, the linear plate bending problem is *per se* an important mathematical model for practical applications and deserves a special treatment. In Section 5, we discuss the specification of the boundary conditions, where we give specific attention to the differences that arise due to boundary layer effects when imposing different constraints for simply supported or clamped conditions. However, to investigate the behavior of the elements in the analysis of general shells and when used in geometrically distorted forms, recourse is necessary to numerical studies. Therefore, we present in Section 6 a selection of numerical results that give insight into the predictive capabilities of the elements discussed in this work.

2. CONTINUUM MECHANICS FORMULATION OF DISPLACEMENT-BASED ELEMENTS

The formulation of the shell elements is based on the use of the general principle of virtual work for 3-D continua modified for the stress-strain and kinematic assumptions of shell behavior. In the following discussion we therefore present first the use of the general principle of virtual work in 3-D large deformation analysis and then discuss the specific modifications used for shell analysis.

2.1 Principle of Virtual Work

The large deformation analysis requires in general a step-by-step incremental solution. The basic continuum mechanics equation used in this solution is the linearized incremental form of the principle of virtual work [29].

To establish the governing equations, we make the fundamental assumption that the response of the continuum can be described by the incremental potential,

$$d\,{}_0^tW = {}_0^t\tilde{S}^{ij}\, d\,{}_0^t\tilde{\epsilon}_{ij} \tag{1}$$

where the ${}_0^t\tilde{S}^{ij}$ are the contravariant components of the 2nd Piola-Kirchhoff stress tensor and the ${}_0^t\tilde{\epsilon}_{ij}$ are the covariant components of the Green-Lagrange strain tensor, both at time t and referred to the original configuration (that corresponds to time 0). The variable ${}_0^tW$ represents the energy per unit of original volume.

The description postulated in (1) holds, of course, for elastic materials and also for inelastic materials widely considered in engineering practice (for example, von Mises plasticity and creep).

A consequence of the assumption in (1) is that

$$ {}_0^t\tilde{S}^{ij} = \frac{\partial_0^t W}{\partial_0^t \tilde{\epsilon}_{ij}} \tag{2} $$

The principle of virtual work is given as [29]

$$ \int_{^0V} {}_0^t\tilde{S}^{ij}\ \delta_0^t\tilde{\epsilon}_{ij}\ d\ {}^0V = {}^tR \tag{3} $$

where ${}^tR$ is the total external virtual work due to surface and body forces.

Using (2) we can write (3) as

$$ \delta \int_{^0V} {}_0^tW\ d\ {}^0V = {}^tR \tag{4} $$

and it follows that the linearization of the principle of virtual work expression (for the incremental solution) will for deformation-independent loading lead to symmetric tangent stiffness matrices.

If the loading is deformation-dependent (*i.e.*, ${}^tR$ depends on the deformations from time 0 to time t) a non-symmetric contribution to the stiffness matrix may be obtained when linearizing (4).

In fact, Schweizerhof and Ramm [30] have studied the case of pressure loading, that usually leads to a displacement dependent loading. In such cases the pressure is modeled as a follower loading *i.e.*, the direction of the pressure loading is considered to be always normal to the deformed surface on which the pressure is acting. In order to briefly outline how a follower pressure loading is introduced in the formulation, consider that part of the total external virtual work ${}^tR$ is due to the displacement dependent pressure loading, and denote it by ${}^tR_p$. Then we can write

$$ {}^tR_p = \int_{^tS_p} {}^tp_i\ \delta u_i\ d\ {}^tS_p \tag{5} $$

where ${}^tS_p$ is the surface area at time "t" on which the pressure is acting and ${}^tp_i$ is the i^{th} component of the pressure which can be defined as

$$ {}^tp_i = {}^t\lambda\ {}^lf\ \ {}^tn_i \tag{6} $$

Here ${}^t\lambda$ is the load multiplier for proportional loading, ${}^lf = {}^lf\ ({}^lx_1, {}^lx_2, {}^lx_3)$ represents the spatial loading distribution and ${}^tn_i$ is the i^{th} component of the unit normal vector to the surface at time t. Regarding ${}^lf$ two cases can be identified. For $l = t$ *i.e.*, ${}^tf = {}^tf\ ({}^tx_1, {}^tx_2, {}^tx_3)$, the pressure loading at time "t" at a particular point depends on the spatial position occupied by the point at time "t". This case is referred to as space attached load. For $l = 0$ *i.e.*, ${}^0f = {}^0f\ ({}^0x_1, {}^0x_2, {}^0x_3)$, the pressure loading at a particular point depends on the position occupied by the point in the initial configuration. This case is referred to as body attached loading.

Due to the displacement dependency of ${}^tR_p$ as given in Eqs. (5) and (6) its incremental loading term will have the usual type of load vector plus a contribution to the tangent stiffness as detailed in [30]. This contribution is in general non–symmetric characterizing a non-conservative type of loading (in some cases, *e.g.*, for particular boundary conditions, this matrix contribution may be symmetric). The purpose of these remarks regarding displacement dependent pressure loading was merely to hint how deformation-dependent loading may lead to non-symmetric contributions to the tangent stiffness matrix.

In practice, it may, however, be more efficient to neglect the non-symmetric stiffness matrix contribution and simply include the deformation dependency of the loading in the iteration vectors.

The incremental form of the principle of virtual work for the stress solution at time $t+\Delta t$ is obtained by performing a Taylor series expansion in terms of the displacements about the state at time t. Then substituting the interpolations for the displacement components as summarized in Section 2.2 yields the equations of motion of a finite element

$$ {}^{t}\underline{K}\ \underline{\hat{u}} = {}^{t+\Delta t}\underline{R} - {}^{t}\underline{F} \tag{7}$$

where $\underline{\hat{u}}$ stores the incremental nodal point displacements (and nodal point rotations in the case of a shell element) and ${}^{t}\underline{K}$ is the tangent stiffness matrix; the vector ${}^{t+\Delta t}\underline{R}$ is the load vector corresponding to time $t+\Delta t$, and ${}^{t}\underline{F}$ is the vector of nodal point forces corresponding to the element stresses at time t. Here

$$ {}^{t}F_i = \frac{\partial}{\partial \hat{u}_i}\left(\int_{{}^0V} {}^{t}_{0}W \ d\,{}^0V\right) \tag{8}$$

$$ {}^{t}K_{ij} = \frac{\partial {}^{t}F_i}{\partial \hat{u}_j} \tag{9}$$

and using chain differentiation

$$ {}^{t}F_i = \int_{{}^0V} {}^{t}_{0}\tilde{S}^{kl}\frac{\partial {}^{t}_{0}\tilde{\epsilon}_{kl}}{\partial \hat{u}_i} d\,{}^0V \tag{10}$$

$$ {}^{t}K_{ij} = \int_{{}^0V} {}_{0}C_{klrs}\frac{\partial {}^{t}_{0}\tilde{\epsilon}_{kl}}{\partial \hat{u}_i}\frac{\partial {}^{t}_{0}\tilde{\epsilon}_{rs}}{\partial \hat{u}_j} d\,{}^0V + \int_{{}^0V} {}^{t}_{0}\tilde{S}^{kl}\frac{\partial^2\ {}^{t}_{0}\tilde{\epsilon}_{kl}}{\partial \hat{u}_i\,\partial \hat{u}_j} d\,{}^0V \tag{11}$$

In the analysis of continua using isoparametric finite elements the displacements are interpolated in a fixed Cartesian coordinate system as

$$ {}^{t}u_i = h_L\ {}^{t}u_i^L \tag{12}$$

where ${}^{t}u_i^L$ is the nodal point displacement in the coordinate direction i at node L and time t. Also

$$ {}^{t}_{0}\tilde{\epsilon}_{kl} = \frac{1}{2}\left({}^{t}_{0}x_{b,k}\ \ {}^{t}_{0}x_{b,l} - \delta_{kl}\right) \tag{13}$$

where ${}^{t}_{0}x_{b,l} = \frac{\partial^t x_b}{\partial^0 x_l}$ and δ_{kl} is the Kronecker delta . Hence

$$ \frac{\partial\ {}^{t}_{0}\tilde{\epsilon}_{kl}}{\partial u_i^L} = \frac{1}{2}\left({}^{t}_{0}x_{i,k}\ \ {}_{0}h_{L,l}\ +\ {}^{t}_{0}x_{i,l}\ {}_{0}h_{L,k}\right) \tag{14}$$

and

$$ \frac{\partial^2\ {}^{t}_{0}\tilde{\epsilon}_{kl}}{\partial u_i^L \partial u_j^M} = \frac{1}{2}\left({}_{0}h_{L,k}\ {}_{0}h_{M,l}\ +\ {}_{0}h_{L,l}\ {}_{0}h_{M,k}\right)\delta_{ij} \tag{15}$$

where the u_i^L, u_i^M are the incremental nodal point displacements identified earlier as $\hat{u}_i$. In the analysis of shells we use

$$ {}^{t}_{0}\tilde{\epsilon}_{kl} = \frac{1}{2}\left({}^{t}\underline{g}_k\ \cdot\ {}^{t}\underline{g}_l\ -\ {}^{0}\underline{g}_k\ \cdot\ {}^{0}\underline{g}_l\right) \tag{16}$$

where

$$ {}^{t}\underline{g}_i = \frac{\partial\, {}^{t}\underline{x}}{\partial r_i}, \quad {}^{0}\underline{g}_i = \frac{\partial\, {}^{0}\underline{x}}{\partial r_i} \tag{17} $$

and $r_1 \equiv r, r_2 \equiv s$ and $r_3 \equiv t$ where (r, s, t) are the usual isoparametric coordinates . In this case the $\hat{u}_i$ correspond to translational and rotational degrees of freedom; hence the differentiations required in (10) and (11) are more difficult to evaluate and depend on the specific rotational degrees of freedom used.

2.2 Shell Assumptions

The assumptions used for the shell kinematic and stress conditions are a generalization of the Reissner-Mindlin plate theory [29].

Figure 3 shows a typical shell to be analyzed. The kinematics of the shell are described by the motion of the shell mid-surface and the motion of the director vector ${}^{t}\underline{V}_n$ which is defined for each material point of the mid-surface: the origin of the vector is at the mid-surface of the shell and usually the vector is initially normal to this mid-surface. During the shell deformations the vector translates and rotates, and if initially normal to the shell mid-surface it may not remain so.

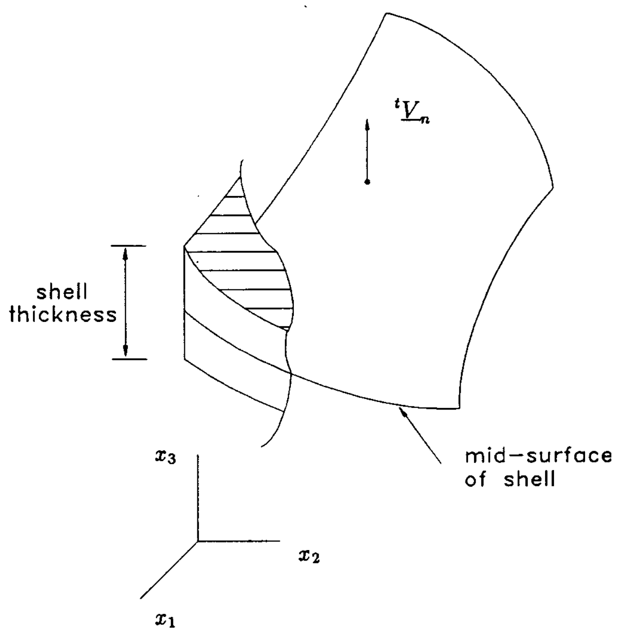

Figure 3. A piece of a typical shell

To describe the motion of the director vector we use the three Cartesian displacements of the vector origin – which are also used to describe the motion of the shell mid-surface – and the direction cosines of the vector. The displacements and rotations of the shell can be small or large, but the fundamental assumption is that the particles lying originally on the director vector will continue to lie on that vector throughout the motion.

Regarding the stress conditions we assume that the Cauchy stresses in the direction of the director vector are initially zero and remain zero throughout the motion of the shell. Hence, plane stress conditions with the direction "normal to the plane" defined by the director vector are assumed.

3. DISPLACEMENT–BASED SHELL ELEMENTS

The formulation of the displacement-based shell elements is based on the principle of virtual work with the kinematic and stress assumptions summarized above, and on the interpolation of the coordinates of the material particles of the shell.

3.1 Interpolation of Coordinates and Displacements

Figure 4 shows a typical shell element. The coordinates of any material particle at time t are [29]

$$ {}^t x_i = h_k \; {}^t x_i^k + \frac{t}{2} \; a_k \; h_k \; {}^t V_{ni}^k \tag{18} $$

where the h_k are the usual 2-D isoparametric interpolation functions in (r, s), a_k is the thickness of the element at node k measured along the direction of the director vector, the ${}^t x_i^k$ are the coordinates of the nodal point k and the ${}^t V_{ni}^k$ are the direction cosines of the director vector ${}^t \underline{V}_n^k$ at the nodal point k. We note that the material particle coordinates, the nodal point coordinates and the directions of the director vectors are all measured in the stationary coordinate system, x_i, $i = 1, 2, 3$. For the element in Figure 4 the number of nodes is sixteen and hence in Eq. (18) $k = 1, \ldots, 16$.

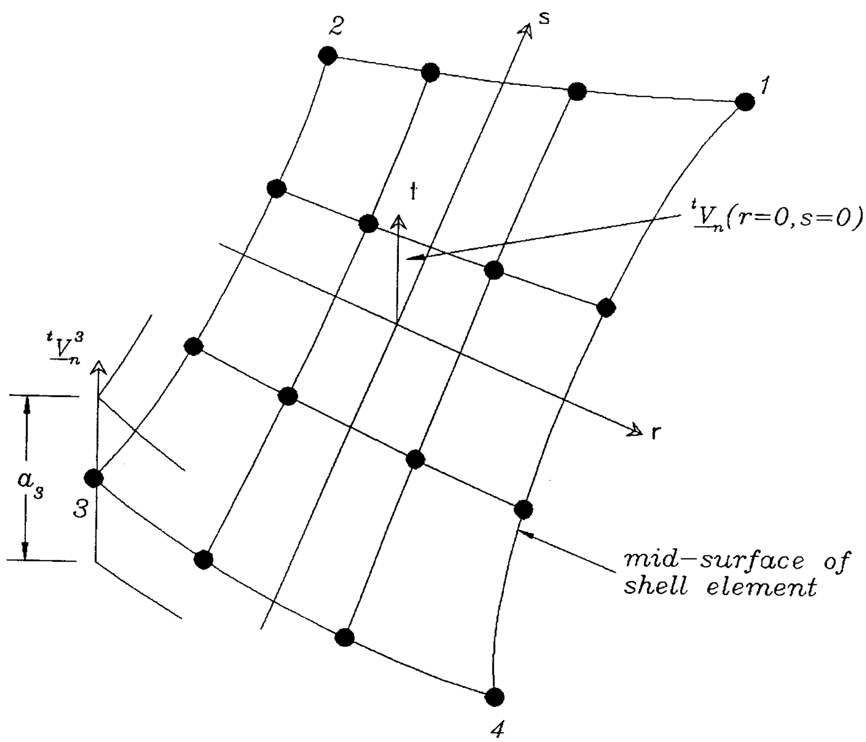

Figure 4. Typical shell element. The direction of the isoparametric coordinate t is given by the director vector ${}^t\underline{V}_n(r, s)$

Equation (18) and Figure 4 show that the shell element geometry is interpolated using the intrinsic coordinate variables r, s and t. We note that the variable $t, -1 \le t \le 1$, is measured in the direction of the director vector ${}^t\underline{V}_n$ and the variables r and $s, -1 \leq r, s \leq +1$, are measured in the mid-surface of the shell element.

For the definition of the stress-strain law, the direction of "zero normal stress" is taken to be the t-direction and the stress-strain law at any material particle is established in the $(\overline{r}, \overline{s}, t)$ system, where unit vectors in these directions are

$$\underline{e}_{\overline{r}} = (\underline{e}_s \times \underline{e}_t) \, / \, \parallel \underline{e}_s \times \underline{e}_t \parallel_2 \tag{19}$$

$$\underline{e}_{\overline{s}} = \underline{e}_t \times \underline{e}_{\overline{r}} \tag{20}$$

and $\underline{e}_r$, $\underline{e}_s$, $\underline{e}_t$ are the unit vectors in the r, s and t directions.

It is clear that with the coordinate interpolation for any time t given by Eq. (18), the displacements at any time can directly be evaluated; for example,

$${}^t u_i = {}^t x_i \; - \; {}^0 x_i \tag{21}$$

$$= h_k \; {}^t u_i^k + \frac{t}{2} a_k h_k \left({}^t V_{ni}^k \; - \; {}^0 V_{ni}^k \right) \tag{22}$$

In the finite element formulation we linearize the response about the configuration at time t (see Eqs. (10) and (11)) and want to use nodal point displacements and rotations. Hence, we need to relate the change in ${}^t\underline{V}_n^k$ to rotations at the nodal point k. This is achieved by introducing two auxiliary axes ${}^t\underline{V}_1^k$ and ${}^t\underline{V}_2^k$ which together with ${}^t\underline{V}_n^k$ form an orthonormal basis at the nodal point k, see Figure 5, and by measuring the rotations α_k and β_k about these axes [29, 9]. The kinematics of large rotations then give that the director vector at time $t + \Delta t$ can be written as [29, 31].

$${}^{t+\Delta t}\underline{V}_n^k = {}^{t+\Delta t}_{\;\;t}\underline{R}_k \; {}^t\underline{V}_n^k \tag{23}$$

where ${}^{t+\Delta t}_{\;\;t}\underline{R}_k$ is a rotation matrix,

$${}^{t+\Delta t}_{\;\;t}\underline{R}_k = \underline{I} + \frac{\sin\theta_k}{\theta_k}\underline{\Theta}_k + \frac{1}{2}\frac{\sin\left(\frac{\theta_k}{2}\right)^2}{\left(\frac{\theta_k}{2}\right)^2}\left(\underline{\Theta}_k\right)^2 \tag{24}$$

with

$$\theta_k = \left[\alpha_k^2 + \beta_k^2\right]^{\frac{1}{2}} \tag{25}$$

$$\underline{\Theta}_k = \begin{bmatrix} 0 & 0 & \beta_k \\ 0 & 0 & -\alpha_k \\ -\beta_k & \alpha_k & 0 \end{bmatrix} \tag{26}$$

In practice, the vectors ${}^t\underline{V}_1^k$, ${}^t\underline{V}_2^k$ and ${}^t\underline{V}_n^k$ are established in the initial configuration (*i.e.* for time $t = 0$) and then the vectors are updated in the incremental solution assuring that they remain an orthonormal basis throughout the deformations of the element [32].

With the kinematic and stress behavior defined as above, the expressions (10) and (11) can directly be evaluated to obtain the tangent incremental equilibrium equations of the shell element.

We should note that the solution of the Eq. (7) yields incremental nodal point variables that – because of the linearization about the configuration at time t – are an approximation to the exact solution for the incremental displacements and rotations from time t to time $t + \Delta t$. Hence, in general, this solution is used to enter into an equilibrium iteration [29]. In the full Newton-Raphson method the stiffness matrix would be updated in each iteration providing quadratic convergence because a consistent linearization of the governing Eq. (3) is used.

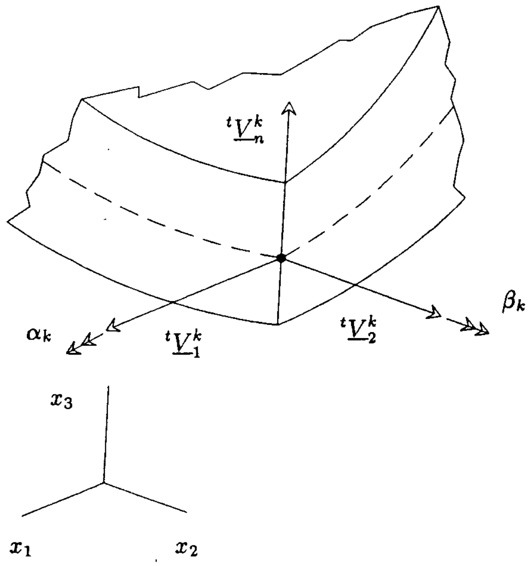

Figure 5. Definition of rotational degrees of freedom α_k and β_k

3.2 Nodal Point Variables

The nodal point variables in the solution are the incremental displacements into the Cartesian coordinate directions and the rotations α_k and β_k about the current ${}^t\underline{V}_1^k$ and ${}^t\underline{V}_2^k$ axes. We note that these axes change direction during the large displacement motion.

There are hence five natural nodal point variables at each shell node. However, some special considerations are necessary at shell nodes,

(i) that are shared by two or more shell elements,
(ii) that connect also to other kinds of finite elements, or
(iii) at which rotational boundary conditions (rotations or moments) are prescribed.

Namely, at these nodes it may be more convenient to use six degrees of freedom.

Consider case (i). If a single director vector is used at the shell node shared by two or more shell elements, only five degrees of freedom describe the kinematic behavior (since no stiffness is calculated for the rotation about the director vector ${}^t\underline{V}_n^k$). In practice, the user would prescribe that only five degrees of freedom shall be used at such a node and the program would automatically assign only a single director vector (as the average of the vectors normal to the mid-surfaces of the shell elements at that node). If a smooth shell surface is modeled, the assumption of a single director vector at the node is quite appropriate (see Figure 6a). However, at a node of a corner or edge of shell surfaces, a single director vector may not represent the desired model (see Figure 6b) and here the analysis could employ different director vectors for each element. This requires the use of six degrees of freedom at the node (see Figure 6c). In practice, the user would assign six degrees of freedom at a corner or edge node if the model of Figure 6.c is to be used, and the program would then establish automatically different director vectors for each element at that node.

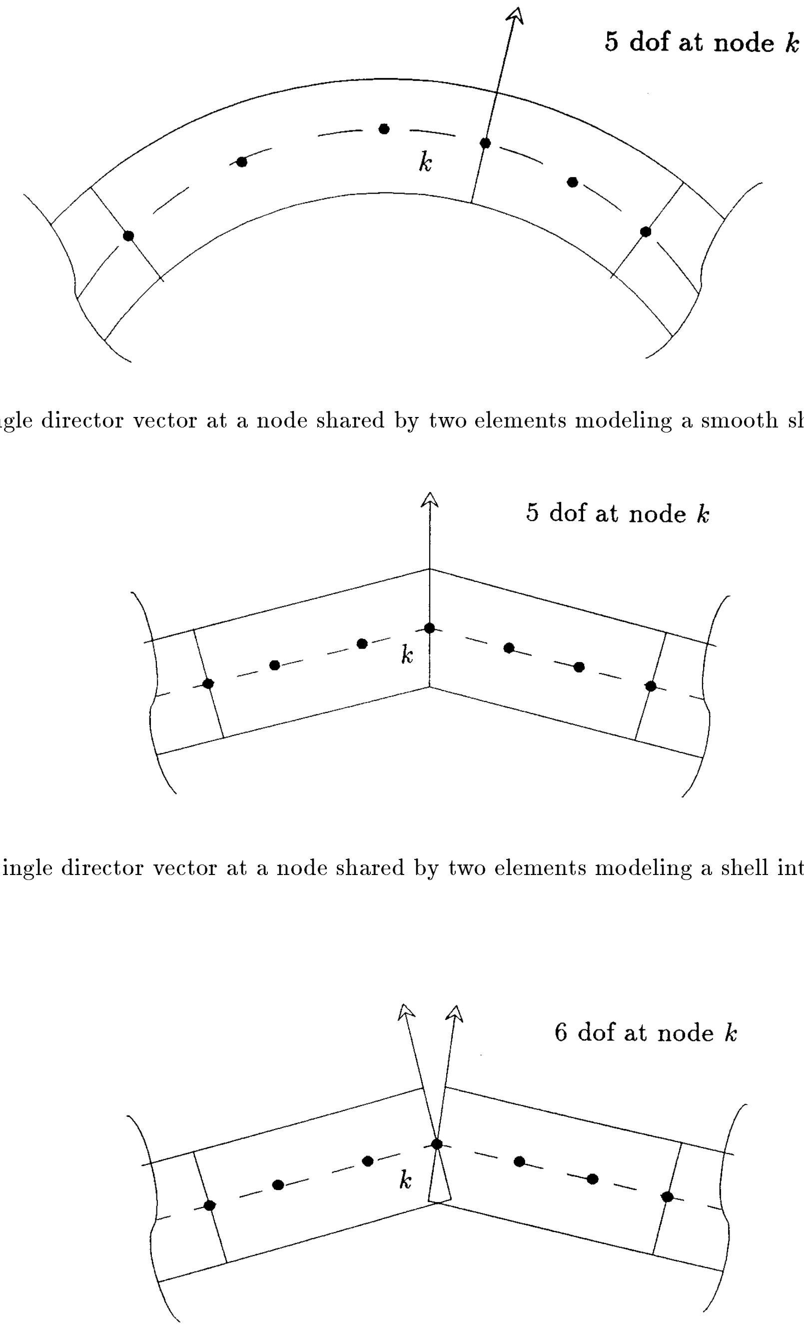

(a) Single director vector at a node shared by two elements modeling a smooth shell surface

(b) Single director vector at a node shared by two elements modeling a shell intersection

(c) Element individual director vectors at a node shared by two shell elements modeling a shell intersection

Figure 6. Director vector at nodes shared by elements

Considering cases (ii) and (iii) the use of six degrees of freedom at the shell node may be necessary because in (ii) the other finite elements (e.g., beam elements) may carry rotational degrees of freedom in three global (or skew) coordinate directions and in (iii) specific rotational boundary conditions in global (or skew) coordinate directions may need to be imposed (for example, to enforce symmetry conditions). In each of these cases it is however important when building the model to keep in mind that the shell element has only rotational stiffness about its ${}^t\underline{V}_1^k$ and ${}^t\underline{V}_2^k$ axes.

Another convenient way to model shell intersections, such as the intersection schematically displayed in Figure 6b, is to use transition elements. These elements [29, 33] are formulated with shell mid-surface nodes and top and bottom surface nodes. The shell mid-surface nodes carry the usual shell degrees of freedom whereas the top and bottom surface nodes carry only translational degrees of freedom. Solutions with these transition elements can also yield more accurate results [33].

3.3 Element Performance

The above displacement formulation is applicable to elements with a varying number of nodes. However, in practice, only the cubic 16-node quadrilateral element, referred to as the 16-node displacement-based element, or higher order elements, can be used for general shell analysis, because the lower-order elements "lock" due to spurious shear and membrane strains. Even the 16-node displacement-based element can show a locking behavior. The 16-node displacement-based element when distorted and/or curved can display a poor predictive capability for coarse meshes. This is due largely to the effects of membrane and shear locking that are increasingly important as the element is curved and distorted.

Shear locking is due to the inability of the elements (with the finite element interpolation used) to represent the condition of zero transverse shear strains *and* still preserve enough element degrees of freedom to permit a good approximation.This condition of zero transverse shear strains is progressively enforced in the finite element solutions as the thickness of the plate/shell becomes smaller, being totally enforced in the limit. When the only finite element solution that satisfies the zero shear strain condition corresponds to zero nodal displacements everywhere the overstiffening of the solutions can be very large even for finite thicknesses. A classical example of this situation is the case when lower-order elements are subjected to a bending moment only.

Even in the cases where zero shear strains can be represented with non-zero nodal displacement, convergence may become very slow since the restricted finite element space that leads to zero shear stresses may be much smaller than the original finite element space.

Membrane locking appears in curved structures due to the inability of the elements to represent zero membrane states. Membrane locking will be an issue in cases when the limit solution(thickness tending to zero) corresponds to zero membrane strains.

As already mentioned, membrane locking occurs, of course, only in curved elements. However, in geometrically nonlinear analysis, elements which are initially flat may become significantly curved during the incremental solution and may therefore only membrane lock as the deformations increase.

In the above discussion we assumed that the element stiffness matrices are evaluated with "full" numerical integration: this order of numerical integration is such that for geometrically undistorted elements the exact stiffness matrices are calculated. If this same integration order is used to evaluate the stiffness matrices of geometrically distorted elements, the error in the numerical evaluation is not very significant as long as the element distortions are reasonable. To relieve the "locking" behavior of the low-order displacement-based shell elements, relatively simple schemes of reduced and selective numerical integration have been proposed [10, 12]. Such approaches lead to computational efficiency in the evaluation of the element stiffness matrix and also to overall solution effectiveness in the analysis of certain problems. However, if, as already mentioned in the Introduction, an element stiffness matrix contains a spurious zero energy mode (such as reported in [34]) the element is interesting for research purposes but unacceptable for practical analysis because it is not reliable.

To suppress the spurious zero energy modes, Belytschko and co-workers proposed a numerical control that can lead to efficient solutions and that has also been related to a variational basis [15, 16]. A shortcoming of these elements is that numerical control parameters have to be selected and that their performance is quite sensitive to element geometric distortions.

An effective approach to formulate reliable and quite efficient lower-order shell elements is to use a mixed interpolation on strains and displacements. This approach is closely related to mixed and hybrid formulations but it is computationally much more effective. To construct general elements, Bathe and Dvorkin introduced a mixed interpolation on the tensorial components of displacements and strains [21, 2] and arrived at a 4-node and a 8-node element that do not shear or membrane lock, that do not contain spurious zero energy modes and that display good accuracy characteristics in general analysis. Similar formulative approaches were then also used for example by Huang and Hinton [35], Park and Stanley [36] and Jang and Pinsky [37] to propose nine node shell elements. Huang and Hinton used a local Cartesian system to separate bending and membrane strains and mixed-interpolated only the membrane part. The transverse shear strains were evaluated and mixed-interpolated in the natural co-ordinate system. Park and Stanley used assumed physical strain component fields that were derived from special assumptions on the strains along selected coordinate lines. Jang and Pinsky assumed covariant strain components in natural coordinates for both the in-layer and transverse shear strains. These approaches of formulation are similar to the approach used in [16] and also in this work, but the actual detailed assumptions employed results, of course, in quite different elements.

Recently, Bucalem and Bathe [38] proposed two additional elements based on the mixed interpolation of the tensorial components, a 9-node element and a 16-node element, that display the numerical efficiency and reliability of the 4-node and 8-node elements mentioned above.

4. MIXTED INTERPOLATION

4.1 Mixed Interpolated General Shell Elements

We stated in Section 3 that the governing equations of the displacement-based shell elements are obtained by introducing the kinematic shell behavior through the finite element interpolations assumptions, both for the geometry and for the displacement variables in the evaluation of the covariant strain components ${}_0^t\tilde{\epsilon}_{ij}$. The tangent stiffness matrix ${}^tK_{ij}$ may then be readily obtained using Eq. (11). However, as has already been pointed out, the resulting element formulations display membrane and shear locking behavior.

The key step of the mixed interpolation of the tensorial components approach is to define assumed strain component fields that are linked with the displacement variables and that lead to element formulations that are free from membrane and shear locking difficulties.

In order to make precise the mixed formulation let us denote by ${}_0^t\tilde{\epsilon}_{ij}^{DI}$ the strain components obtained from the finite element interpolation assumptions both for the geometry and displacement variables. The superscript DI stand for "**d**irect" **i**nterpolation using the geometry and displacement finite element interpolation assumptions. The mixed interpolated elements are constructed using ${}_0^t\tilde{\epsilon}_{ij}^{AS}$in place of ${}_0^t\tilde{\epsilon}_{ij}^{DI}$, where the superscript AS indicates that **a**ssumed **s**train fields are used.

The definition of how the assumed strain fields relate to the directly interpolated strain fields actually characterizes a particular element formulation. The success or failure of an element formulation in avoiding membrane and shear locking is entirely related to the definition of the assumed strain fields and how they relate to the usual strain fields.

For the plate bending problem a mathematical theory guides the selection of appropriate assumed strain fields. The discussion of these mathematical ideas will be developed to some extent in Section 4.2. Besides guiding the construction of optimally convergent plate bending elements this mathematical theory provides much understanding and insight into the shear locking phenomenon.

The mixed interpolated shell finite elements that will be presented here have been developed based on insight into element behavior and the use of numerical experimentation.

Let us consider the construction of the assumed strain fields for specific elements. We omit temporarily, merely for ease of notation, the subscripts and superscripts relating to times $(0, t)$ in the strain expressions.

We use the convected coordinate system that is defined element-wise by the element isoparametric coordinates r, s and t as shown in Figure 3 with the following convention for indicial notation: $r_1 \equiv r, r_2 \equiv s$ and $r_3 \equiv t$.

Considering the kinematical shell assumptions implicitly defined in Eq. (18), the strain tensor can be written as

$$\begin{aligned} \underline{\epsilon}^{DI} = \tilde{\epsilon}_{rr}^{DI}\, \underline{g}^r \underline{g}^r + \tilde{\epsilon}_{ss}^{DI}\, \underline{g}^s \underline{g}^s + \tilde{\epsilon}_{rs}^{DI} \left(\underline{g}^r \underline{g}^s + \underline{g}^s \underline{g}^r \right) + \\ + \ \tilde{\epsilon}_{rt}^{DI} \left(\underline{g}^r \underline{g}^t + \underline{g}^t \underline{g}^r \right) + \tilde{\epsilon}_{st}^{DI} \left(\underline{g}^s \underline{g}^t + \underline{g}^t \underline{g}^s \right) \end{aligned} \tag{27}$$

or

$$\underline{\epsilon}^{DI} = \underline{\epsilon}_{IL}^{DI} + \underline{\epsilon}_{RT}^{DI} + \underline{\epsilon}_{ST}^{DI} \tag{28}$$

where $\underline{\epsilon}_{IL}^{DI}$ is the in-layer part of the strain tensor and $\underline{\epsilon}_{RT}^{DI}$ and $\underline{\epsilon}_{ST}^{DI}$ the transverse shear strain parts, with the following definitions:

$$\underline{\epsilon}_{IL}^{DI} = \tilde{\epsilon}_{rr}^{DI}\, \underline{g}^r \underline{g}^r + \tilde{\epsilon}_{ss}^{DI}\, \underline{g}^s \underline{g}^s + \tilde{\epsilon}_{rs}^{DI} \left(\underline{g}^r \underline{g}^s + \underline{g}^s \underline{g}^r \right) \tag{29}$$

$$\underline{\epsilon}_{RT}^{DI} = \tilde{\epsilon}_{rt}^{DI} \left(\underline{g}^r \underline{g}^t + \underline{g}^t \underline{g}^r \right) \tag{30}$$

$$\underline{\epsilon}_{ST}^{DI} = \tilde{\epsilon}_{st}^{DI} \left(\underline{g}^s \underline{g}^t + \underline{g}^t \underline{g}^s \right) \tag{31}$$

One way of defining a mixed interpolation of the strains is to use the previous decomposition and write $\underline{\epsilon}^{AS}$, the assumed strain tensor as,

$$\underline{\epsilon}^{AS} = \underline{\epsilon}_{IL}^{AS} + \underline{\epsilon}_{RT}^{AS} + \underline{\epsilon}_{ST}^{AS} \tag{32}$$

where $\underline{\epsilon}_{IL}^{AS}$ is the assumed in-layer strain part and $\underline{\epsilon}_{RT}^{AS}$ and $\underline{\epsilon}_{ST}^{AS}$ are the assumed transverse shear strain parts.

Each assumed strain part is obtained by evaluating the corresponding directly interpolated strain part at some selected points, called tying points, and interpolating from these values to define the assumed strain tensor part for any point in the element domain.

The MITC8 element is formulated with this approach and the details of this formulation will shortly become apparent when we present the element.

Of course, to arrive at the stiffness matrix using Eq. (11) each particular assumed covariant strain component can be evaluated using

$$\tilde{\epsilon}_{ij}^{AS} = \underline{g}_i \cdot \underline{\epsilon}^{AS} \cdot \underline{g}_j \tag{33}$$

Another approach that has been used to formulate mixed interpolated shell elements is to define assumed strain fields for each covariant strain component. In fact, for each strain component $\tilde{\varepsilon}_{ij}$ we define a set of points, $k = 1, \ldots, n_{ij}$, by specifying for each point k its natural coordinates $r = r_k$, $s = s_k$ and t. These points are also called tying points.

Now the assumed covariant strain component $\tilde{\varepsilon}_{ij}^{AS}$ is defined as

$$\tilde{\varepsilon}_{ij}^{AS}(r,s,t) = \sum_{k=1}^{n_{ij}} h_k^{ij}(r,s)\, \tilde{\varepsilon}_{ij}^{DI}(r_k, s_k, t) \tag{34}$$

where $h_k^{ij}(r,s)$ are interpolation functions (polynomials in r and s) associated with the strain component $\tilde{\varepsilon}_{ij}$ such that

$$h_k^{ij}|^l := h_k^{ij}(r_l, s_l) = \delta_{kl}, \quad l = 1, \dots, n_{ij} \tag{35}$$

and denoting

$$\tilde{\varepsilon}_{ij}^{DI}|^k := \tilde{\varepsilon}_{ij}^{DI}(r_k, s_k, t) \quad \text{and} \quad \tilde{\varepsilon}_{ij}^{AS}|^k := \tilde{\varepsilon}_{ij}^{AS}(r_k, s_k, t) \tag{36}$$

it follows

$$\tilde{\varepsilon}_{ij}^{AS}|^k = \tilde{\varepsilon}_{ij}^{DI}|^k, \quad k = 1, \dots, n_{ij} \tag{37}$$

Of course, this selection is the reason why the n_{ij} points are called tying points.

4.1.1 The MITC8 element

The MITC8 element construction follows the first approach, outlined in the previous section, *i.e.,* assumed strain fields are defined considering the interpolation of the in-layer and transverse shear strain parts.

The assumed in-layer strain fields are defined by

$$\underline{\epsilon}_{IL}^{AS} = \sum_{k=1}^{8} h_k^{IL} \underline{\epsilon}_{IL}^{DI} \,|^k \tag{38}$$

where the h_k^{IL} are the usual 8-node element interpolation functions corresponding to the points $k = 1, ..., 8$ identified in Figure 7a and for $k = 1, \dots, 4$

$$\underline{\epsilon}_{IL}^{DI} \,|^k = \tilde{\epsilon}_{rr}^{DI} \underline{g}^r \underline{g}^r \,|^k + \tilde{\epsilon}_{ss}^{DI} \underline{g}^s \underline{g}^s \,|^k + \tilde{\epsilon}_{rs}^{DI} \left(\underline{g}^r \underline{g}^s + \underline{g}^s \underline{g}^r \right) |^k$$

For $k = 5$ and 7

$$\begin{aligned} \underline{\epsilon}_{IL}^{DI} \,|^5 = {} & \tilde{\epsilon}_{ss}^{DI} \underline{\bar{g}}^s \underline{\bar{g}}^s \,|^5 + \left\{ \underline{\bar{g}}_r \cdot \left[\frac{1}{2} \left(\underline{\epsilon}^{DI} \,|^1 + \underline{\epsilon}^{DI} \,|^2 \right) \right] \cdot \underline{\bar{g}}_r \right\} \underline{\bar{g}}^r \underline{\bar{g}}^r \,|^5 \\ & + \left\{ \underline{\bar{g}}_r \cdot \left[\frac{1}{2} \left(\underline{\epsilon}^{DI} \,|^1 + \underline{\epsilon}^{DI} \,|^2 \right) \right] \cdot \underline{\bar{g}}_s \right\} \left(\underline{\bar{g}}^r \underline{\bar{g}}^s + \underline{\bar{g}}^s \underline{\bar{g}}^r \right) |^5 \end{aligned} \tag{39}$$

$$\begin{aligned} \underline{\epsilon}_{IL}^{DI} \,|^7 = {} & \tilde{\epsilon}_{ss}^{DI} \underline{\bar{g}}^s \underline{\bar{g}}^s \,|^7 + \left\{ \underline{\bar{g}}_r \cdot \left[\frac{1}{2} \left(\underline{\epsilon}^{DI} \,|^3 + \underline{\epsilon}^{DI} \,|^4 \right) \right] \cdot \underline{\bar{g}}_r \right\} \underline{\bar{g}}^r \underline{\bar{g}}^r \,|^7 \\ & + \left\{ \underline{\bar{g}}_r \cdot \left[\frac{1}{2} \left(\underline{\epsilon}^{DI} \,|^3 + \underline{\epsilon}^{DI} \,|^4 \right) \right] \cdot \underline{\bar{g}}_s \right\} \left(\underline{\bar{g}}^r \underline{\bar{g}}^s + \underline{\bar{g}}^s \underline{\bar{g}}^r \right) |^7 \end{aligned} \tag{40}$$

where

$$\underline{\bar{g}}_s \equiv \underline{g}_s ; \underline{\bar{g}}_t \equiv \underline{g}_t \tag{41}$$

$$\underline{\bar{g}}_r = \underline{g}_r - \alpha \underline{g}_s ; \ \alpha = \frac{g_{rs}}{g_{ss}} \tag{42}$$

and for $i = 6$ and 8

$$\underline{\epsilon}_{IL}^{DI}|^6 = \tilde{\epsilon}_{rr}^{DI}\underline{\overline{g}}^r\underline{\overline{g}}^r|^6 + \left\{\underline{\overline{g}}_s \cdot \left[\frac{1}{2}\left(\underline{\epsilon}^{DI}|^2 + \underline{\epsilon}^{DI}|^3\right)\right] \cdot \underline{\overline{g}}_s\right\}\underline{\overline{g}}^s\underline{\overline{g}}^s|^6 + \\ + \left\{\underline{\overline{g}}_r \cdot \left[\frac{1}{2}\left(\underline{\epsilon}^{DI}|^2 + \underline{\epsilon}^{DI}|^3\right)\right] \cdot \underline{\overline{g}}_s\right\}\left(\underline{\overline{g}}^r\underline{\overline{g}}^s + \underline{\overline{g}}^s\underline{\overline{g}}^r\right)|^6 \tag{43}$$

$$\underline{\epsilon}_{IL}^{DI}|^8 = \tilde{\epsilon}_{rr}^{DI}\underline{\overline{g}}^r\underline{\overline{g}}^r|^8 + \left\{\underline{\overline{g}}_s \cdot \left[\frac{1}{2}\left(\underline{\epsilon}^{DI}|^1 + \underline{\epsilon}^{DI}|^4\right)\right] \cdot \underline{\overline{g}}_s\right\}\underline{\overline{g}}^s\underline{\overline{g}}^s|^8 + \\ + \left\{\underline{\overline{g}}_r \cdot \left[\frac{1}{2}\left(\underline{\epsilon}^{DI}|^1 + \underline{\epsilon}^{DI}|^4\right)\right] \cdot \underline{\overline{g}}_s\right\}\left(\underline{\overline{g}}^r\underline{\overline{g}}^s + \underline{\overline{g}}^s\underline{\overline{g}}^r\right)|^8 \tag{44}$$

where

$$\underline{\overline{g}}_r \equiv \underline{g}_r; \underline{\overline{g}}_t \equiv \underline{g}_t \tag{45}$$

$$\underline{\overline{g}}_s = \underline{g}_s - \beta\underline{g}_r; \ \beta = \frac{g_{rs}}{g_{rr}} \tag{46}$$

This interpolation avoids membrane locking and does not introduce spurious zero energy modes.

The assumed shear strains are defined by

$$\tilde{\epsilon}_{rt}^{AS}\underline{g}^r\underline{g}^t = \sum_{k=1}^{4} h_k^{RT}\ \tilde{\epsilon}_{rt}^{DI}\ \underline{g}^r\underline{g}^t|^k + h_5^{RT}\left[\frac{1}{2}\left(\tilde{\epsilon}_{rt}^{DI}|^{RA} + \tilde{\epsilon}_{rt}^{DI}|^{RB}\right)\right]\underline{g}^r\underline{g}^t|^5 \tag{47}$$

and

$$\tilde{\epsilon}_{st}^{AS}\underline{g}^s\underline{g}^t = \sum_{k=1}^{4} h_k^{ST}\ \tilde{\epsilon}_{st}^{DI}\ \underline{g}^s\underline{g}^t|^k + h_5^{ST}\left[\frac{1}{2}\left(\tilde{\epsilon}_{st}^{DI}|^{SA} + \tilde{\epsilon}_{st}^{DI}|^{SB}\right)\right]\underline{g}^s\underline{g}^t|^5 \tag{48}$$

with the interpolation functions $h_k^{RT}$and h_k^{ST} corresponding to the points in Figure 7. Note that in (47) and (48) the mean values of the covariant strain components sampled at points RA and RB , and SA and SB , are used for the fifth interpolation functions. This corresponds to some degree to the theoretical prediction that for high-order elements weighted integrals of the transverse shear strain components should be effective in tying the strain interpolations to the nodal point variables (see Section 4.2).

The above shear strain interpolation prevents shear locking and also does not result into spurious zero energy modes. The element stiffness matrix is evaluated using 3×3 Gauss integration corresponding to the r- and s- directions.

4.1.2 The MITC4, MITC9 and MITC16 elements

In the formulation of the MITC4, MITC9 and MITC16 elements the assumed strain fields are defined as in Eq. (34). Therefore, each covariant strain component has its own interpolation and tying scheme.

For the MITC4 element, only the transverse shear strains are mixed interpolated and the tying points are shown in Figure 8. We note that the selection of the tying points completely defines the assumed interpolation scheme, since the $h_k^{ij}(r,s)$ functions are products of Lagrange polynomials with the property given in (35). The MITC4 element formulation fully fits the framework of element construction described in this section in which each individual covariant strain component is interpolated because, regarding the interpolation of the in-layer strains, we could formally say that the assumed strain fields for the in-layer strains are identical to the directly interpolated strain fields.

The choice of tying points for the 9-node element is given in Figure 9 and the choice for the 16-node element is presented in Figure 10.

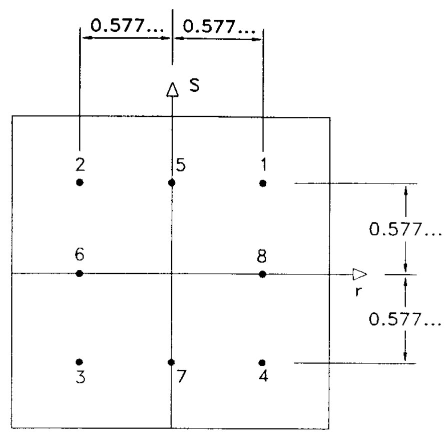

(a) In-layer interpolation tying points. Interpolation functions correspond to eight node interpolation points 1, ······ , 8

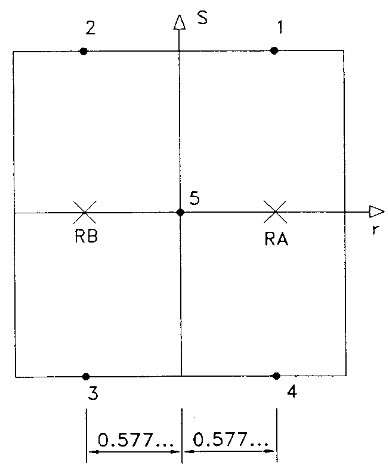

(b) Transverse shear strain interpolations $\tilde{\epsilon}_{rt}\underline{g}^r\underline{g}^t$; five interpolation points

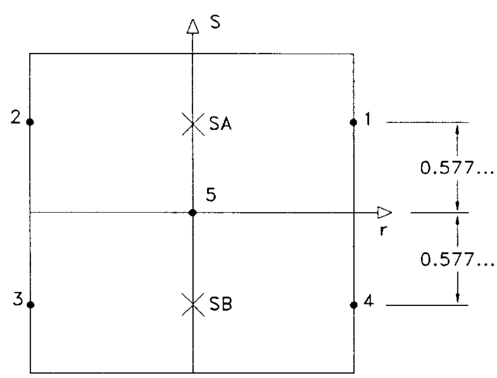

(c) Transverse shear strain interpolations $\tilde{\epsilon}_{st}\underline{g}^s\underline{g}^t$; five interpolation points

Figure 7. Interpolation points for MITC8 element

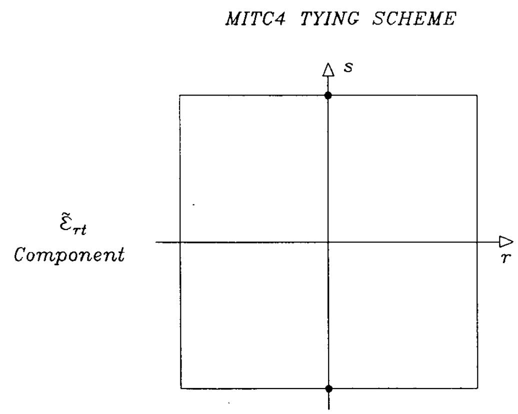

Figure 8. Tying scheme used for the transverse shear strain component $\tilde{\epsilon}_{rt}$ of the MITC4 shell element. Tying scheme for the component $\tilde{\epsilon}_{st}$ is implied by symmetry

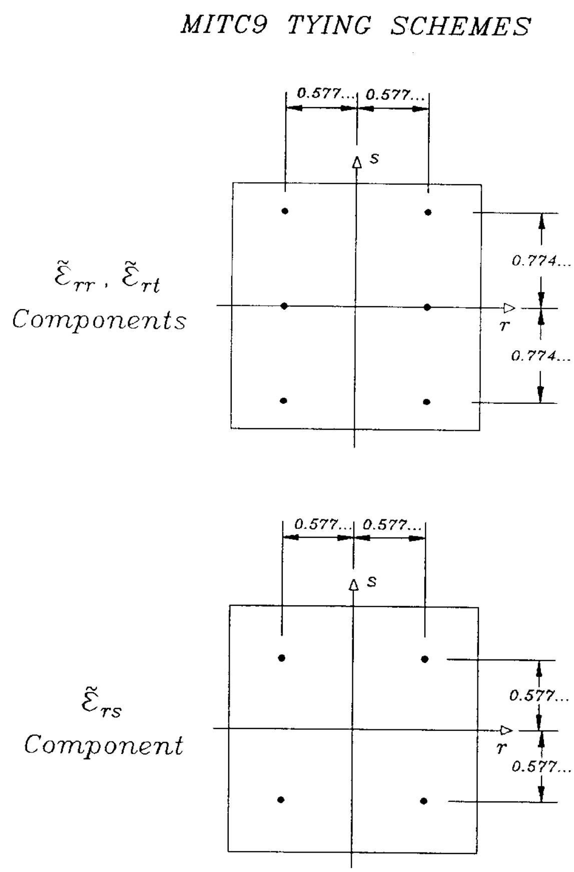

Figure 9. Tying scheme used for the strain components of the MITC9 shell element. Tying scheme for the components $\tilde{\epsilon}_{ss}$ and $\tilde{\epsilon}_{st}$ are implied by symmetry. Coordinates of tying points always coincide with one-dimensional Gauss point coordinates, e.g., $\frac{1}{\sqrt{3}} = 0.577\ldots$

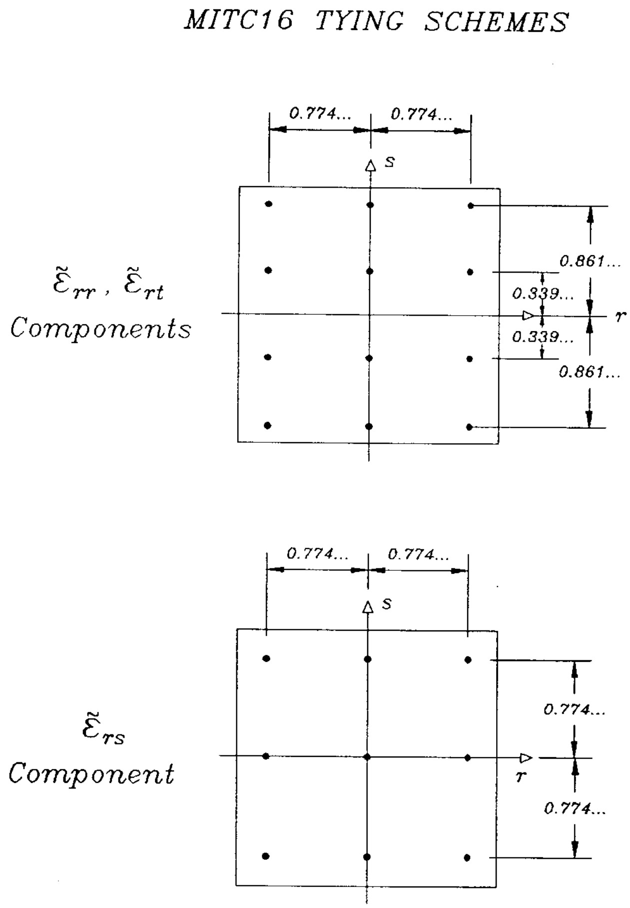

Figure 10. Tying scheme used for the strain components of the MITC16 shell element. Tying scheme for the components $\tilde{\epsilon}_{ss}$ and $\tilde{\epsilon}_{st}$ are implied by symmetry. Coordinates of tying points always coincide with one-dimensional Gauss point coordinates, e.g., $\sqrt{3/5} = 0.774\ldots$

We remark that using the tying points of Figure 9 it is also possible to propose an 8-node element. This element was implement and tested, but it was not sufficiently effective and reliable. Although it performed quite well in some cases, in a few analyses the element presented a very stiff behavior rendering it not useful. This result underlines the importance of the MITC8 element.

It was also assumed for the transverse shear strain components that

$$\tilde{\epsilon}_{rt}\,(r,s,t) = \tilde{\epsilon}_{rt}\,(r,s,0)$$

$$\tilde{\epsilon}_{st}\,(r,s,t) = \tilde{\epsilon}_{st}\,(r,s,0)$$

These elements do not have any spurious zero-energy mode and their stiffness matrices are evaluated with "full" numerical integration, i.e., in the rs plane, 2×2 Gauss integration, for the MITC4 element, 3×3 for the MITC9 element, and 4×4 for the MITC16 element. According to the numerical results, these elements are free of locking and perform quite effectively.

4.2 Additional MITC Elements. The Mixed Interpolated Plate Bending Elements

The MITC4 and MITC8 elements have been constructed by insight into the predictive behaviors to reach 4- and 8-node shell elements that are reliable and have good predictive capabilities. The convergence behavior of the elements was originally tested by considering patch tests and selected plate and shell analyses.

The development of the MITC9 and MITC16 shell elements, that followed, was guided to some extent by the previous developments of the MITC9 and MITC16 plate bending elements. The construction of the MITC plate bending elements involves the definition of assumed transverse shear strain fields and also of tying schemes that relate the assumed and directly interpolated shear strains.

When developing general mixed interpolated shell elements it is also necessary to define assumed transverse shear strain fields and tying conditions. These constructions can be guided by the analogous constructions for the plate bending elements. However, two comments are in order

(i) The plate bending elements were designed to take into account the known nature of the Reissner-Mindlin plate bending mathematical model. When considering general curved shells the mathematical model is quite different and it is not clear whether the optimal choice of assumed transverse shear strain fields is the same as for the plate model.

(ii) As will be reviewed shortly the MITC plate bending element constructions for the higher-order elements require the use of different sets of degrees of freedom for the nodal point displacements and the nodal point section rotations. These constructions, if followed strictly when formulating shell elements, would lead to shell elements that are difficult to use in practical engineering applications. Also, for the MITC plate bending elements not only point-tying conditions are used but also integral-tying conditions. Integral-tying conditions are expensive, in terms of the computational effort, in particular if implemented for shell analysis.

Therefore it is justified that the assumed shear strain fields for the MITC plate and shell elements are not exactly the same. However, it is apparent that the study of the transverse shear strain fields for the plate elements provides valuable insight for developing the corresponding strain fields for shell elements.

Of course, the construction of assumed in-layer strain interpolations can not be aided by the consideration of plate bending analysis. In order to arrive at the assumed in-layer strain interpolations for the MITC9 and MITC16 shell elements insight into element behavior and numerical experimentation were used.

In the remaining part of this section we summarize the fundamental ideas of the mathematical analysis of the Reissner-Mindlin linear elastic plate bending problem. We also present, briefly, the MITC plate elements that have been developed. Some numerical results obtained with these elements are shown as well to indicate the predictive capabilities of these elements.

The mathematical analysis proceeds by considering the minimization of the total potential corresponding to bending of a Reissner- Mindlin plate

$$\inf \left\{ \frac{t^3}{2} a\left(\underline{\beta},\underline{\beta}\right) + \frac{\lambda t}{2} \left\| \underline{\beta} - \underline{\nabla} w \right\|_0^2 - t^3 \left(f, w\right) \right\} \tag{49}$$

$$\underline{\beta} \in \underline{B}; \quad w \in W$$

where $\underline{B}$ is the space of plate section rotations and W is the space of the plate transverse displacement, t is the thickness of the plate and $t^3 f$ is the transverse applied loading. The first term in (49) is the bending strain energy and the second term corresponds to the transverse shear strain energy. If we look for a solution in the finite element subspaces $\underline{B}_h \subset \underline{B}$ and $W_h \subset W$, we know that in general shear locking occurs.

To avoid shear locking we need to reduce the influence of the shear strain energy, and this is achieved by using a space of assumed transverse shear strains $\underline{\Gamma}_h$ and a projection operator R that relates the shear strains given by $\underline{\beta}_h - \underline{\nabla} w_h$ to the assumed strains $R(\underline{\beta}_h - \underline{\nabla} w_h)$ in $\underline{\Gamma}_h$. We assume further that this operator R satisfies

$$R\, \underline{\nabla} w_h = \underline{\nabla} w_h \text{ for all } w_h \in W_h \tag{50}$$

and then solve instead of the discrete version of (49) the following minimization problem

$$\inf \left\{ \frac{t^3}{2} a\left(\underline{\beta}_h, \underline{\beta}_h\right) + \frac{\lambda t}{2} \left\| R\underline{\beta}_h - \underline{\nabla} w_h \right\|_0^2 - t^3\left(f, w_h\right) \right\} \tag{51}$$

$$\underline{\beta}_h \in \underline{B}_h; \quad w_h \in W_h$$

Let us consider the sequence of problems P_t each associated with a particular thickness t, given by

$$P_t : \inf \left\{ \frac{1}{2} a\left(\underline{\beta}, \underline{\beta}\right) + \frac{\lambda t^{-2}}{2} \left\| \underline{\beta} - \underline{\nabla} w \right\|_0^2 - \ (f, w) \right\} \tag{52}$$

$$\underline{\beta} \in \underline{B}; \quad w \in W$$

and analogously the sequence corresponding to (51)

$$P_{th} : \inf \left\{ \frac{1}{2} a\left(\underline{\beta}_h, \underline{\beta}_h\right) + \frac{\lambda t^{-2}}{2} \left\| R\underline{\beta}_h - \underline{\nabla} w_h \right\|_0^2 - \ \left(f, w_h\right) \right\} \tag{53}$$

$$\underline{\beta}_h \in \underline{B}_h; \quad w_h \in W_h$$

Of course, we now have to select $\underline{B}_h, W_h, \underline{\Gamma}_h$ and the operator R such that (53) yields finite element solutions that are convergent to the solution of the continuous problem governed by (52).

Although we would like to consider the convergence of the solution of (53) to (52) for a range of values t physically possible, in order to choose the variables $\underline{B}_h, W_h, \underline{\Gamma}_h$ and R it is expedient to consider the limit case of $t = 0$. The convergence analysis is then, of course, not complete but it does yield important information on what finite element spaces and operators R will be effective.

Therefore, for the limit problem, (52) becomes

$$\inf_{\underline{\beta} = \underline{\nabla} w} \left\{ \frac{1}{2} a\left(\underline{\beta}, \underline{\beta}\right) - \ (f, w) \right\} \tag{54}$$

and (53) becomes

$$\inf_{R\underline{\beta}_h = \underline{\nabla} w_h} \left\{ \frac{1}{2} a\left(\underline{\beta}_h, \underline{\beta}_h\right) - \ \left(f, w_h\right) \right\} \tag{55}$$

Considering the construction of the discrete spaces $\underline{B}_h, W_h, \underline{\Gamma}_h$ we recognize that given a pair $\underline{\beta}$,w of smooth fuctions such that

$$\underline{\beta} = \underline{\nabla} w \tag{56}$$

we want to find a corresponding pair $\underline{\beta}_h \in \underline{B}_h, w_h \in W_h$ such that

$$R(\underline{\beta}_h - \underline{\nabla} w_h) = R\,\underline{\beta}_h - \underline{\nabla} w_h = \underline{0} \tag{57}$$

or

$$R\,\underline{\beta}_h = \underline{\nabla} w_h \tag{58}$$

with $\underline{\beta}_h, w_h$ "close" to $\underline{\beta}, w$ (*i.e.*, $\underline{\beta}_h, w_h$ approximate $\underline{\beta}, w$ with optimal error bounds). If this holds true and if R is "close" to the identity operator, then the solution of (55) will be a good approximation of the solution of (54).

We note that (56) implies

$$rot\left(\underline{\beta}\right) = 0 \tag{59}$$

and analogously (58) implies

$$rot\left(R\underline{\beta}_h\right) = 0 \tag{60}$$

The condition (59) is much like the condition div $\underline{u} = 0$ to be satisfied in the analysis of incompressible media(where $\underline{u}$ is the displacement vector), except that in (59) the *rot* operator is used [39].

Taking advantage of the incompressible analysis problem it can be established that given a continuous field $\underline{\beta}$ such that $rot\ \underline{\beta} = 0$ we can find $\underline{\beta}_h \in \underline{B}_h$ which is a "good" approximation for $\underline{\beta}$ and that

$$\int_\Omega rot(\underline{\beta}_h)\ q_h d\Omega = 0\ \forall q_h \in Q_h \tag{61}$$

where $\underline{B}_h, Q_h$ are a "good" pair of displacement-pressure spaces for the approximation of the incompressible medium problem.

If R and $\underline{\Gamma}_h$ are chosen such that

$$\int_\Omega rot(\underline{\eta})\ q_h d\Omega = \int_\Omega rot(R\underline{\eta})\ q_h d\Omega \tag{62}$$

$$\forall \underline{\eta} \in \underline{B}_h; \quad \forall q_h \in Q_h$$

and if

$$rot\underline{\Gamma}_h \subseteq Q_h \tag{63}$$

then Eq. (61) implies the desired (60).

Considering Eqs.(50) and (58) we realize that there is not much choice left to define W_h. In fact it is necessary that

$$\underline{\nabla} W_h = \left\{\underline{\varphi} \in \underline{\Gamma}_h \text{such that}\ \ rot\underline{\varphi} = 0\right\} \tag{64}$$

This condition together with (50) characterizes W_h.

We note that (64) together with (60) implies the existence of $w_h \in W_h$ such that (58) holds and since R is to be chosen as a good approximation of the identity operator

$$\underline{\nabla} w_h = R\,\underline{\beta}_h \simeq\ \underline{\beta}_h \simeq\ \underline{\beta} = \underline{\nabla} w$$

meaning that w_h will be a good approximation of w.

Therefore the choice of the finite element spaces is guided by the following steps:

Step 1: choose $\underline{B}_h, Q_h$ such that it corresponds to a "good"displacement-pressure pair for the analysis of incompressible media. These pairs can be easily found in the literature (see for example [49]).

Step 2: choose $\underline{\Gamma}_h$and R such that Eqs. (62) and (63) are satisfied.

Step 3: choose W_h according to Eq. (64).

It has been established [19] that the above element construction leads to mixed interpolated plate bending elements that have optimal convergence characteristics and therefore do not lock.

We note that the tying, *i.e.*, the link between the assumed strain fields given by $\underline{\Gamma}_h$ and the directly interpolated strain fields is given by Eq. (62).

The mathematical analysis summarized above has evolved from the analysis of the MITC4 element, that has originally been proposed for shell analysis, when used in plate bending conditions. The elements that have been developed according to the mathematical framework outlined above and that have also been numerically tested are: the MITC9 and the MITC16 elements (quadrilateral 9- and 16-node elements); the MITC7 and MITC12 elements (triangular 7- and 12-node elements). These elements are described in Figures 11, 12, 13, 14 and 15. As we may observe, for the higher-order, MITC7, MITC9, MITC12 and MITC16 elements, different sets of degrees of freedom for transverse displacements and section rotations are used and also integral tying conditions are present. We have already pointed out this fact when discussing the possible differences between MITC plate bending and shell elements and the reasons why they were actually constructed in this way. When the MITC9 and MITC16 shell elements are used under plate bending conditions they do not degenerate to the MITC9 and MITC16 plate bending elements. Of course, we do not expect that the MITC9 and MITC16 shell elements perform as well as the MITC9 and MITC16 plate elements when used for plate bending problems. However, the shell elements should still behave quite effectively in plate bending situations and, of course, not shear lock.

We present below two plate bending problems that have been modeled with the MITC plate elements. A third problem is studied where we compare the behavior of the MITC plate and shell elements in the analysis of a plate bending problem.

4.2.1 Analysis of a simply-supported square plate

We consider the transverse shear stress predictions in the analysis of a square plate subjected to uniform pressure. In this problem the transverse shear stresses display a strong boundary layer [40]. Therefore this is an adequate test problem to assess the predictive capability of the elements regarding transverse shear stresses for engineering problems in which these stresses vary rapidly.

Only a quarter of the plate needs to be discretized and we obtained a reference solution using graded meshes of 16–node displacement based elements (in undistorted form). The 10×10 graded mesh is shown in Figure 16 and the 20×20 mesh was obtained by subdividing each element of the 10×10 mesh into four new elements. The solutions obtained with these meshes showed negligible differences.

In Figures 17 and 18 we show the predictions, along the edge of the plate from the corner, obtained with the MITC4 and MITC9 elements and the reference solution. The stresses are evaluated at the corner of the elements using the $\underline{\Gamma}_h$ spaces. The MITC element predictions show a good convergence to the reference solution. We note that at a sufficient distance from the corner the solution corresponds to the Kirchhoff solution. We also remark that for an accurate solution grading in the meshes should be used for this type of analysis [29].

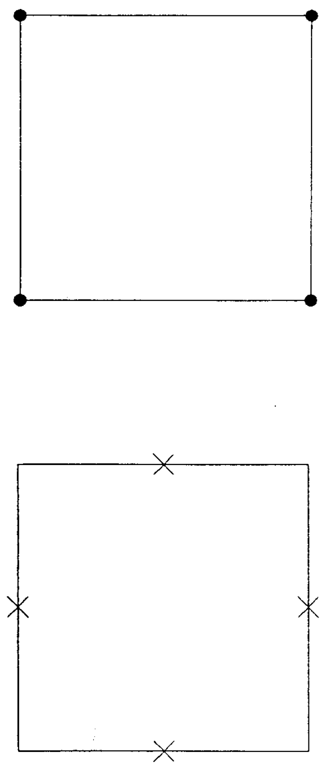

Spaces

$\underset{\sim}{\Theta}_h : Q_1 \times Q_1$

$W_h : Q_1$

$\underset{\sim}{\Gamma}_h : \begin{Bmatrix} a_1+b_1 y \\ a_2+b_1 x \end{Bmatrix}$

Point Tying

$$\int_e (\underset{\sim}{\eta} - R\underset{\sim}{\eta}) \,.\, \underset{\sim}{\tau}\; ds = 0$$

for all edges e of K

Figure 11. MITC4 plate element

4.2.2 Convergence in the analysis of an "Ad-hoc problem"

We consider the problem of a square Reissner-Mindlin plate of side lengths two units, see Figure 19. The interior loading is p=0 and the imposed boundary displacement and section rotations correspond to:

$$w = \sin kx e^{ky} + \sin k e^{-k} \tag{65}$$
$$\beta_x = k \cos kx e^{ky} \tag{66}$$
$$\beta_y = k \sin kx e^{ky} \tag{67}$$

with $k = 5$. We note that the above equations satisfy the Reissner-Mindlin plate equations for any value of the thickness t, and hence represent the complete (boundary and interior) solution. There is no boundary layer [40,41], and indeed the transverse shear strains are zero.

Hence this problem is a valuable test problem in that the numerically calculated convergence rates should be close to the theoretically predicted rates.

Spaces

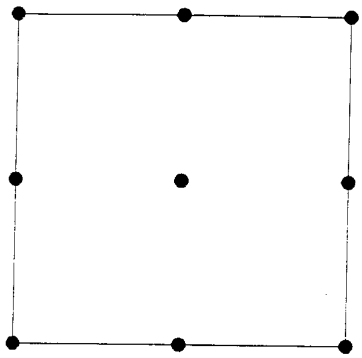

$$\underline{\Theta}_h : Q_2 \times Q_2$$

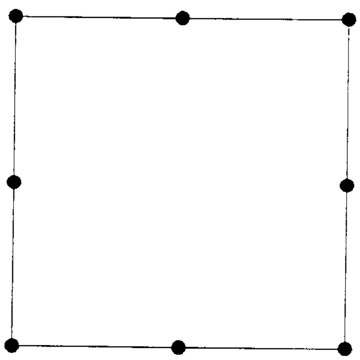

$$W_h : Q_2 \cap P_3$$

$$\underline{\Gamma}_h : \begin{Bmatrix} a_1 + b_1 x + c_1 y + d_1 xy + e_1 y^2 \\ a_2 + b_2 x + c_2 y + d_2 xy + e_2 x^2 \end{Bmatrix}$$

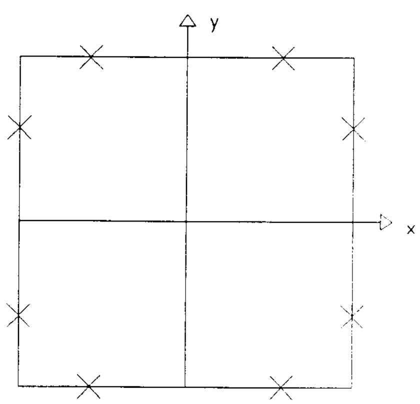

Point Tying

$$\int_e (\underline{\eta} - R\underline{\eta}) \cdot \underline{\tau} \; p_1(s) \;\; ds = 0$$

for all edges e of K, for all $p_1(s) \in P_1(e)$
$\underline{\tau}$ vector tangent to edge e

Integral Tying

$$\int_K (\underline{\eta} - R\underline{\eta}) \quad dK = 0$$

Figure 12. MITC9 plate element

Spaces

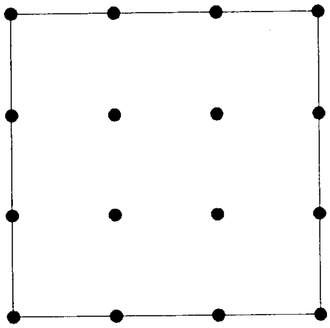

$$\underline{\Theta}_h : Q_3 \times Q_3$$

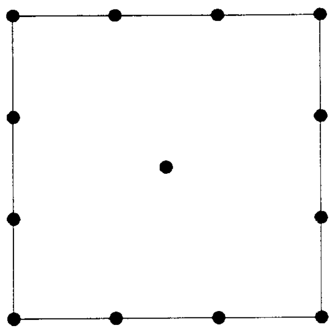

$$W_h : Q_3 \cap P_4$$

$$\underline{\Gamma}_h : \begin{Bmatrix} a_1+b_1x+c_1y+d_1x^2+e_1xy+f_1y^2+g_1x^2y+h_1xy^2+i_1y^3 \\ a_2+b_2x+c_2y+d_2x^2+e_2xy+f_2y^2+g_2x^2y+h_2xy^2+i_2x^3 \end{Bmatrix}$$

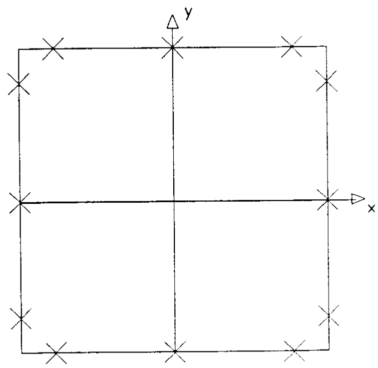

Point Tying

$$\int_e (\underline{\eta} - R\underline{\eta}) \cdot \underline{\tau}\, p_2(s)\ ds = 0$$

for all edges e of K, for all $p_2(s) \in P_2(e)$
$\underline{\tau}$ vector tangent to edge e

Integral Tying

$$\int_K (\underline{\eta} - R\underline{\eta})\ \underline{p}_1 dK,\ \forall\, \underline{p}_1 \in (P_1(K))^2$$

Figure 13. MITC16 plate element

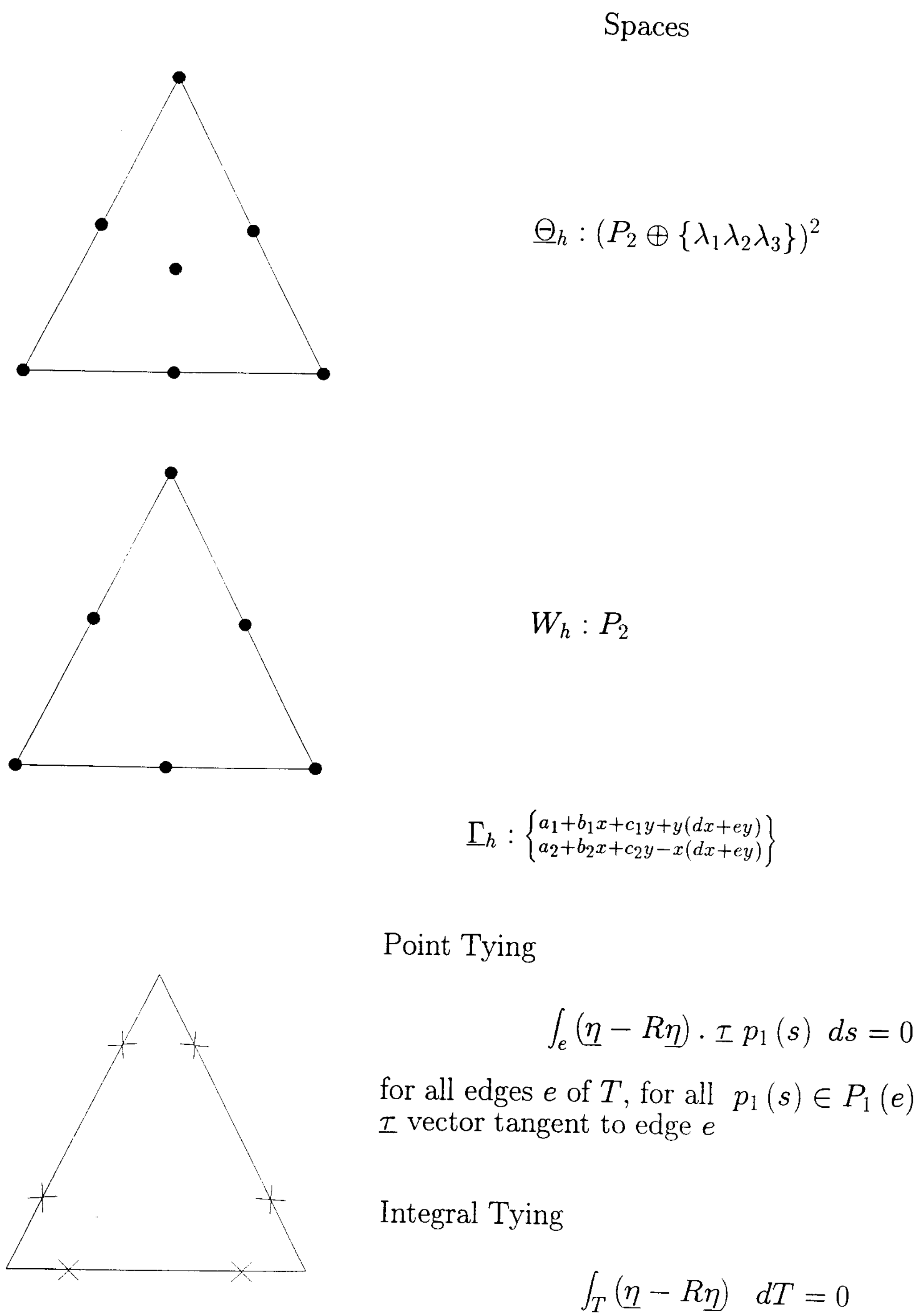

Figure 14. MITC7 plate element

Spaces

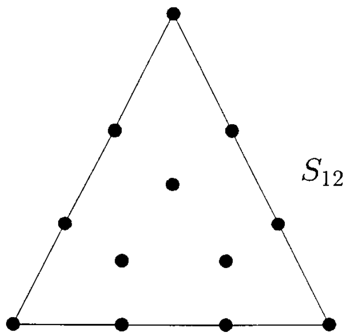

$$\underline{\Theta}_h : \left(S_{12}\left(T\right)\right)^2$$

$$S_{12}\left(T\right) = \{\varphi \mid \varphi \in P_4, \varphi\mid_e \in P_3 \text{ on each edge } e \text{ of } T\}$$

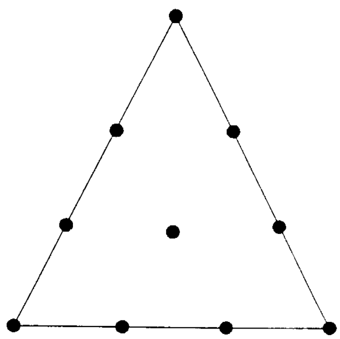

$$W_h : P_3$$

$$\underline{\Gamma}_h : \left\{ \begin{array}{l} a_1+b_1x+c_1y+d_1x^2+e_1xy+f_1y^2+y(gx^2+hxy+iy^2) \\ a_2+b_2x+c_2y+d_2x^2+e_2xy+f_2y^2-x(gx^2+hxy+iy^2) \end{array} \right\}$$

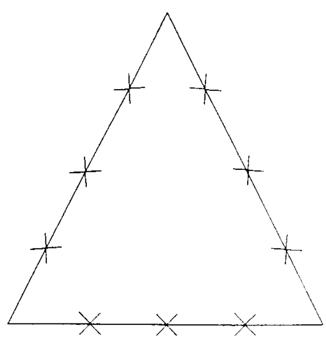

Point Tying

$$\int_e \left(\underline{\eta} - R\underline{\eta}\right) \cdot \underline{\tau}\, p_2\left(s\right)\; ds = 0$$

for all edges e of T, for all $p_2\left(s\right) \in P_2\left(e\right)$
$\underline{\tau}$ vector tangent to edge e

Integral Tying

$$\int_T \left(\underline{\eta} - R\underline{\eta}\right) \cdot \underline{p}_1\; dT = 0, \forall\, \underline{p}_1 \in \left(P_1\left(T\right)\right)^2$$

Figure 15. MITC12 plate element

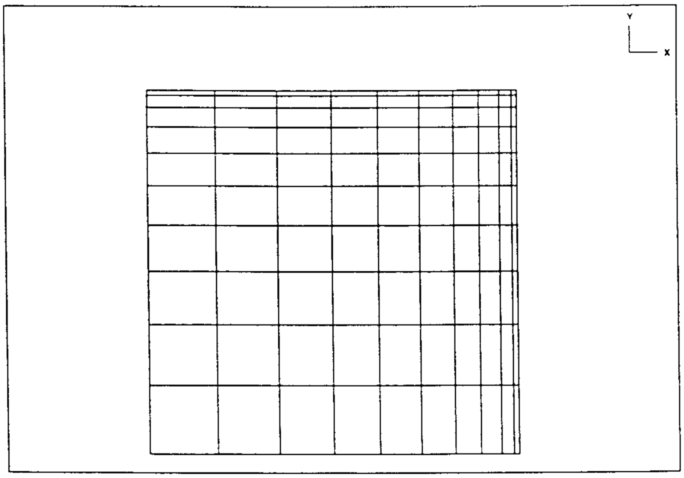

Figure 16. 10 × 10 graded mesh used in the analysis of simply-supported plate, thickness/-length=1/100

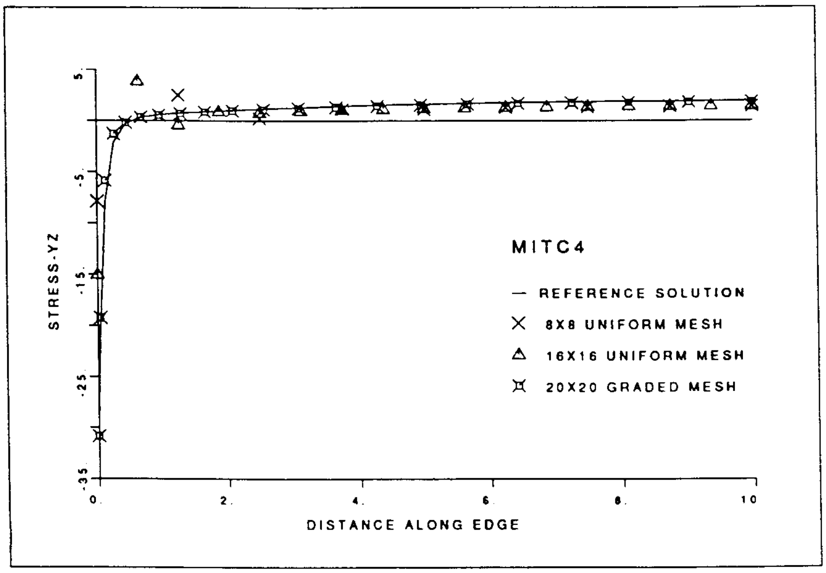

Figure 17. Shear stress predictions near corner of simply-supported plate subjected to pressure loading using MITC4 elements

The plate problem was solved with uniform meshes, where h denotes the side length of each element.

Figures 20, 21 and 22 show the error in the finite element solutions in the Sobolev norms, and the convergence of the transverse shear strains, and Table I gives the average convergence rates. We note that the slopes of the curves in Figures 20, 21 and 22 are in essence constant, and hence the convergence for each element is measured to be quite uniform for each h used.

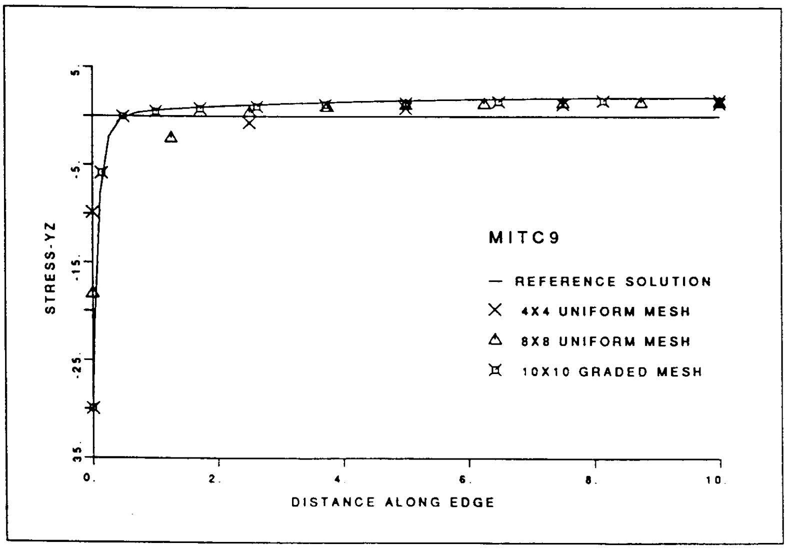

Figure 18. Shear stress predictions near corner of simply-supported plate subjected to pressure loading using MITC9 elements

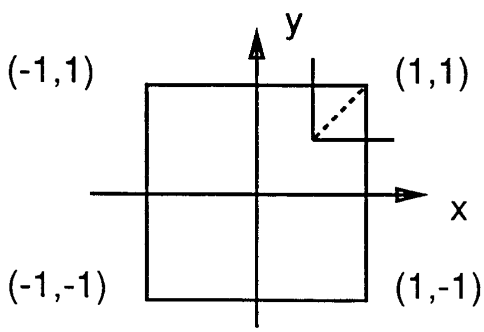

Figure 19. Square plate used in the analysis of ad-hoc problem. The dashed line indicate the subdivision used for triangular elements

Table 1 shows that the numerically obtained convergence rates are quite close to the theoretical rates, and that the convergence of the transverse shear strain components is surprisingly good. The same study was performed with meshes that have been deliberated distorted [25].

The distorted meshes resulted generally into a decrease of the convergence rates, but this decrease was not drastic when considering that rather highly distorted meshes were used, and when taking into account that each mesh contained rather large and small elements.

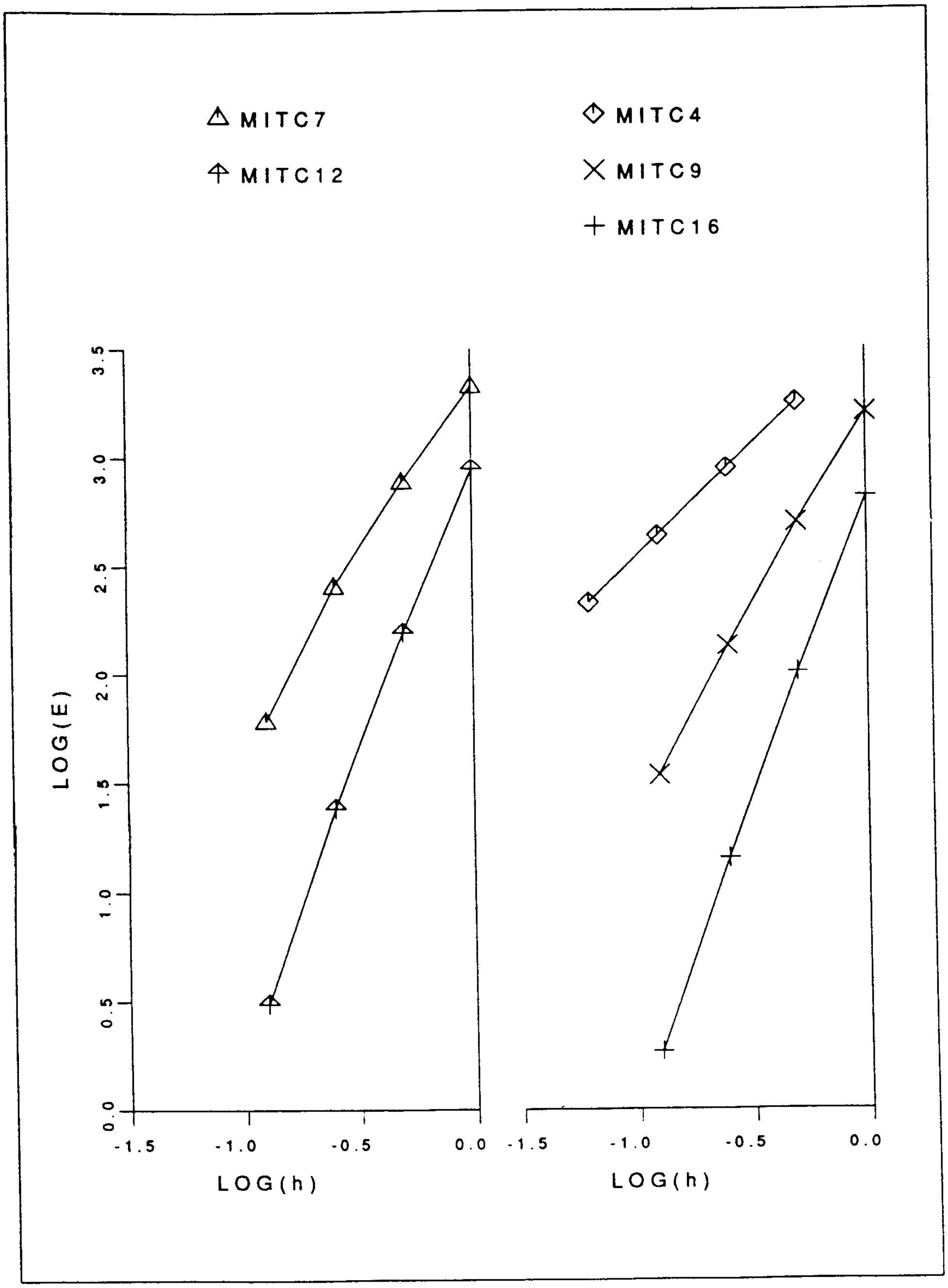

Figure 20. Convergence of section rotations in analysis of ad-hoc problem using uniform meshes. The error measure is $E = \|\underline{\beta} - \underline{\beta}_h\|_1$

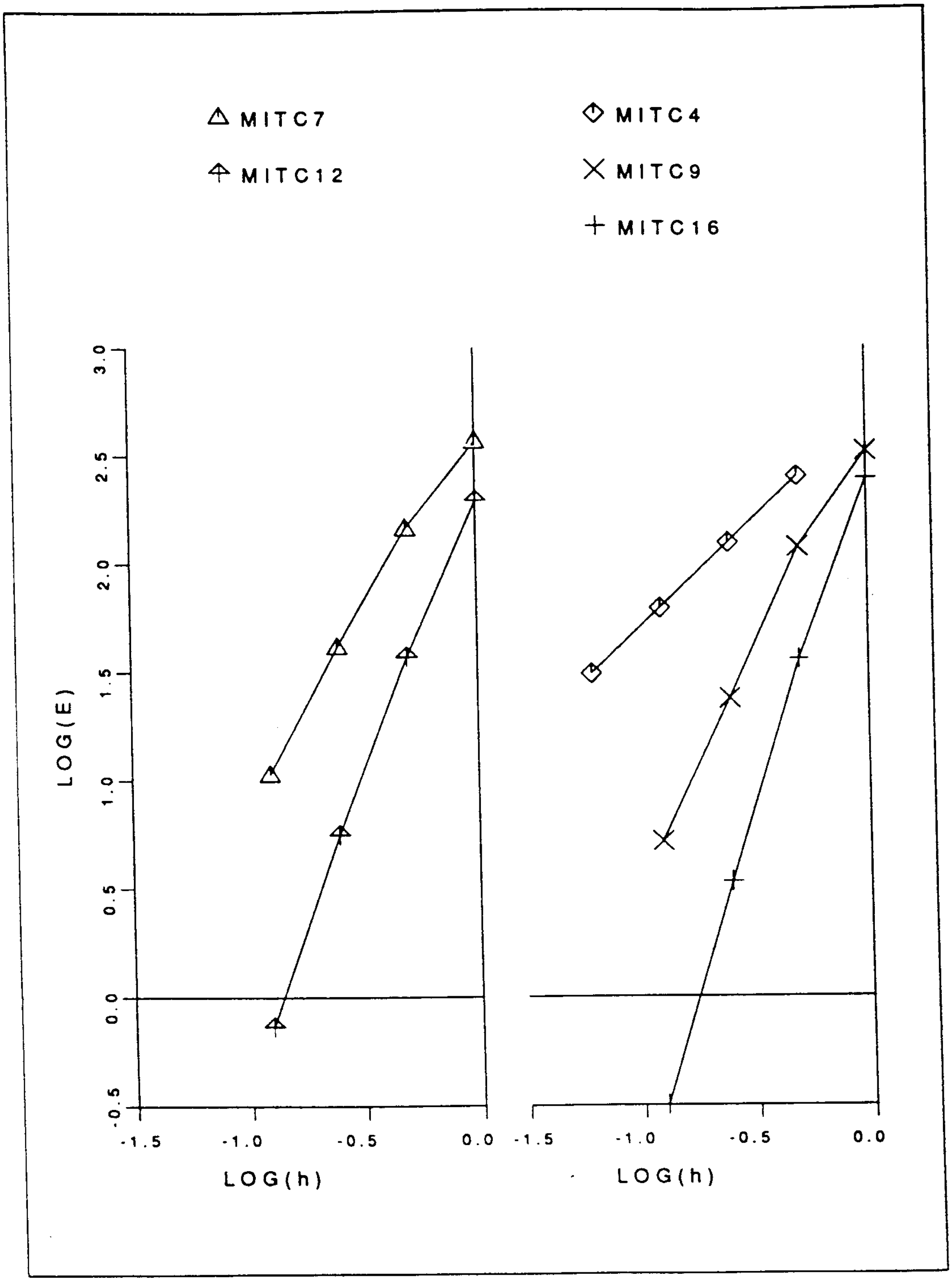

Figure 21. Convergence of gradient of vertical displacement in analysis of ad-hoc problem using uniform meshes. The error measure is $E = \|\underline{\nabla}w - \underline{\nabla}w_h\|_0$

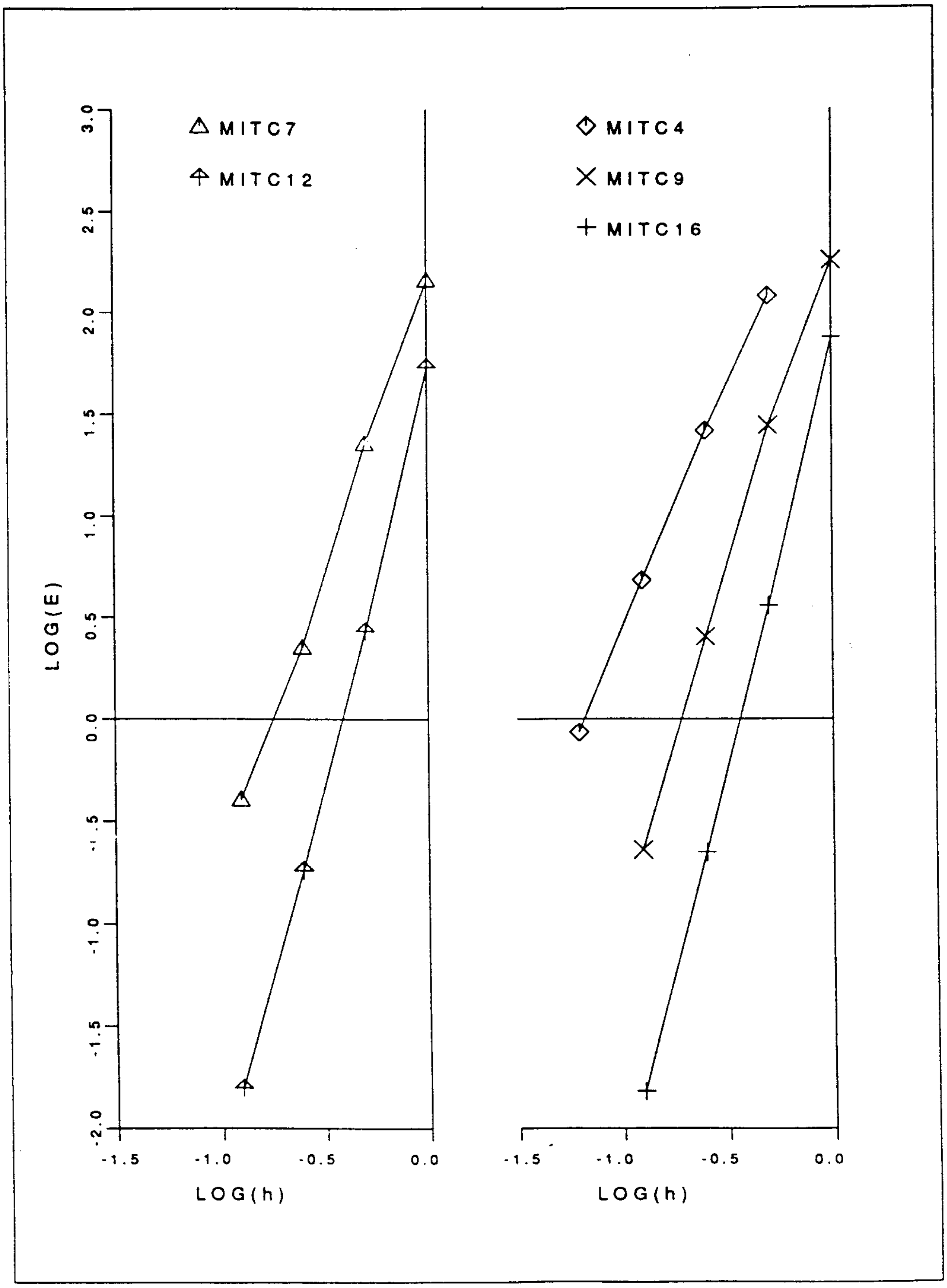

Figure 22. Convergence of transverse shear strains in analysis of ad-hoc problem using uniform meshes. The error measure is $E = \|\underline{\gamma} - \underline{\gamma}_h\|_0$

ELEMENT	$\|\|\underline{\theta} - \underline{\theta}_h\|\|_1$		$\|\|\underline{\theta} - \underline{\theta}_h\|\|_0$	$\|\|\underline{\nabla} w - \underline{\nabla} w_h\|\|_0$		$\|\|w - w_h\|\|_0$	$\|\|\underline{\gamma} - \underline{\gamma}_h\|\|_0$
	Theory	Numerical		Theory	Numerical		
MITC4	1.0	1.0	2.0	1.0	1.0	2.1	2.4
MITC9	2.0	1.8	2.7	2.0	2.0	3.0	3.2
MITC7	2.0	1.7	2.7	2.0	1.7	2.9	2.8
MITC12	3.0	2.7	3.7	3.0	2.7	3.8	3.9
MITC16	3.0	2.8	3.7	3.0	3.2	4.2	4.1

Table 1. Convergence rates obtained in analysis of ad-hoc problem using uniform meshes

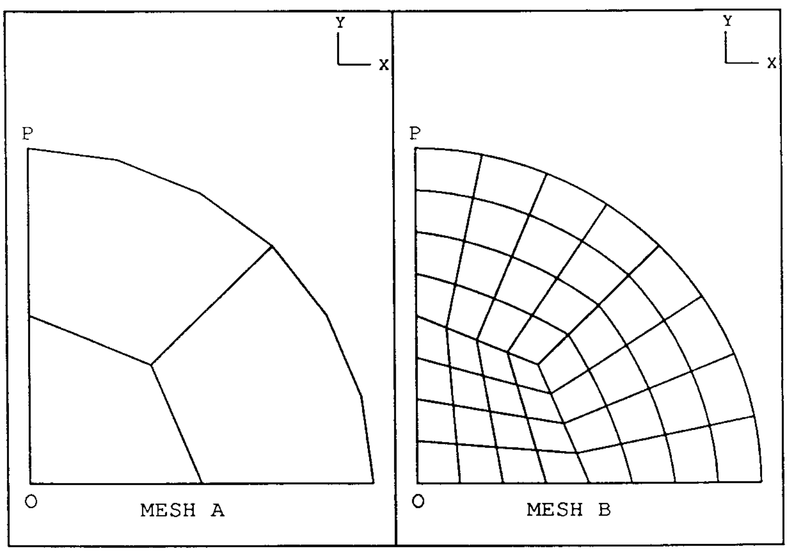

Figure 23. Meshes used in analysis of circular plate, Young's modulus $E = 2.1 \times 10^6$, Poisson's ratio $\nu = 0.3$, pressure $p = 0.03072$, diameter $D = 20.0$

4.2.3 Convergence in the analysis of a circular plate

In this solution we consider a circular plate of thickness t and diameter D. The plate is loaded by a uniform pressure and is simply-supported or clamped along its edge.

Figure 23 gives the data of the problem considered and shows the finite element meshes used. Note that the elements are geometrically distorted in a natural way in order to model the plate.

Of particular interest in this analysis is the prediction of the transverse shear stresses. The analytical solution is rather simple (Figure 24) and there is no boundary layer. Figure 24 shows the calculated stresses as obtained for the simply-supported plate using mesh A for the MITC16 plate and shell elements and the usual 16-node displacement-based element. In this figure we show the stresses calculated at those nodal points along line PO where two elements meet. The stresses for an element at a nodal point have been calculated using for that element

$$\underline{\tau} = \underline{C}\,\underline{\widehat{B}}\,\underline{u} \tag{68}$$

where $\underline{\tau}$ is the vector of the stresses, $\underline{C}$ is the stress-strain matrix, $\underline{\widehat{B}}$ is the strain-displacement matrix of the element at the nodal point considered and $\underline{u}$ is the nodal point displacement vector.

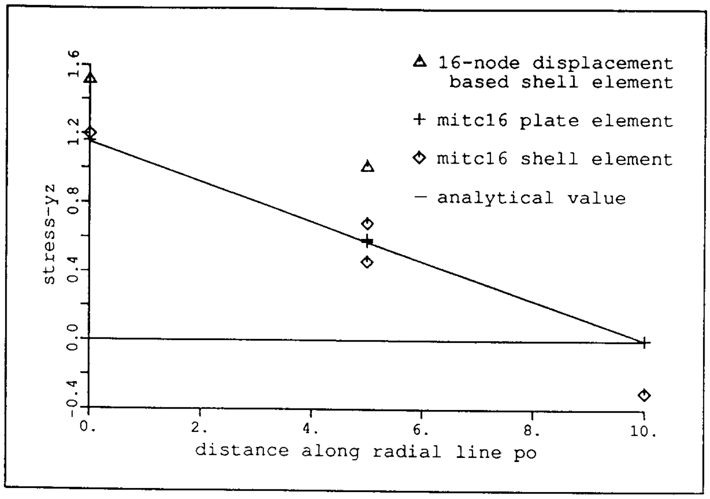

Figure 24. Mesh A shear stress predictions for analysis of simply supported circular plate, diameter/thickness = 100. The results not shown for the 16-node displacement based shell element are actually outside the figure

Hence there is no stress smoothing and at each nodal point where elements meet two values for each shear stress component are obtained.We note that the solution is very accurate using the MITC16 plate element with only three elements. On the other hand, the displacement-based element does not give an accurate transverse shear stress prediction unless a very fine mesh is employed [25]. The MITC16 shell element is not as accurate as the MITC16 plate element, as expected, but it provides good stress predictions considering that the mesh used is quite coarse.

Figure 25 presents the same type of shear stress results using the mesh B shown in Figure 23 and the MITC9 plate and shell elements. A similar behavior as noted for the 16–node elements is encountered.

5. THE SPECIFICATION OF BOUNDARY CONDITIONS

The analysis of a structure requires the imposition of displacement/section rotation boundary conditions and force/moment boundary conditions (also referred to as essential and natural boundary conditions, respectively [29]).

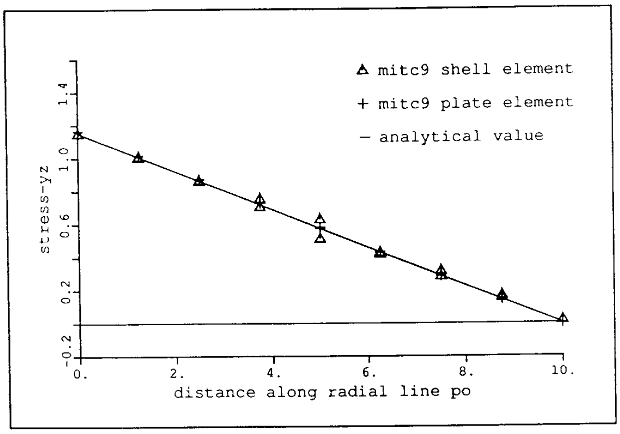

Figure 25. Mesh B shear stress predictions for analysis of clamped circular plate, diameter/thickness = 100

As discussed in Section 3.2, the shell elements presented in this work have five natural stiffness degrees of freedom at a shell node, although when element assemblages are considered the use of six degrees of freedom at a shell node may be appropriate.

The objective in this section is to briefly discuss the imposition of plate and shell geometric boundary conditions. Namely, there are some special considerations that need to be kept in mind when imposing the boundary conditions on the displacement-based or mixed-interpolated elements, and we discuss these in the following by considering the analysis of plates [29, 40, 41].

Consider the skew plate of side lengths L shown in Figure 26. The angle α is a variable so that with $\alpha = \frac{\pi}{2}$ we have a square plate. The thickness of the plate is h. The sides of the plate can be fixed, simply-supported or free of support and the question we ask is how to impose these geometric boundary conditions.

The free support condition means, of course, that the displacement w and the rotations θ_n and θ_s are free along the edge.

The conditions of fixed and simply-supported edges, however, need special considerations.

In Kirchhoff plate theory, a simply-supported edge is modeled by the condition $w = 0$ and this means implicitly that also $\theta_s = 0$. Namely, since $\frac{\partial_w}{\partial_s} = \theta_s$, we have that if $w = 0$ along the edge, θ_s must be zero also. However, in the Reissner-Mindlin plate theory w and θ_s are independent variables and the usual "simple" support is appropriately modeled using only the condition $w = 0$. With this geometric condition, the transverse displacement is zero along the edge, but the section rotations corresponding to θ_s are not necessarily zero.

Therefore, in the finite element solutions of plates using Reissner-Mindlin theory based elements, the nodal transverse displacements should be set equal to zero at simply-supported edges, but the section rotations should usually be left free. These boundary conditions are referred to as "soft-support" boundary conditions. Of course, it would be appropriate to also set the nodal rotations corresponding to θ_s equal to zero if the specific *physical* situation of the simple support is in this way more adequately modeled. This corresponds to the "hard-support" condition, and then restraining moments M_{ns} are generated and the boundary shear stresses are quite different from those calculated when the soft-support condition is assumed.

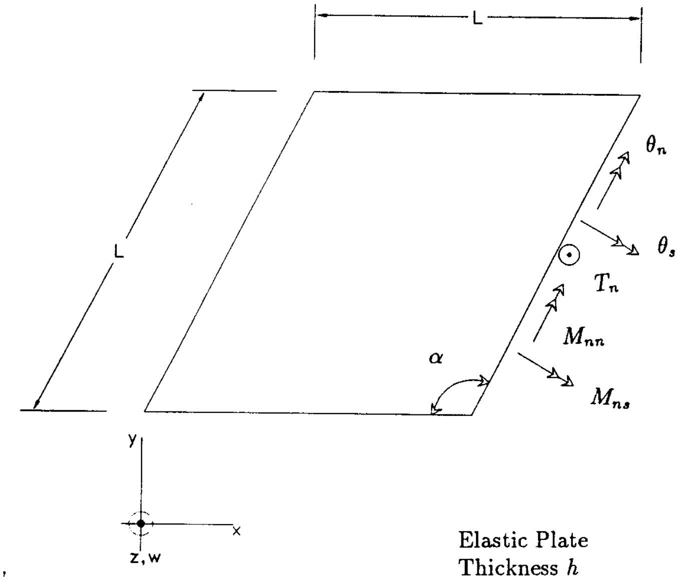

Figure 26. Plane view of plate; T_n is the shearing force

A most interesting phenomenon is that with the soft-support condition the boundary shear stresses approach the Kirchhoff solution through the development of a boundary layer as the thickness of the plate decreases.

Similar observations hold when a fixed edge is considered. Again, the choice of whether to restrain the nodal rotations corresponding to θ_s must be decided depending on the actual physical support to be modeled.

Figure 27 shows the analysis results reported in [40] for the solution of a simply-supported square plate subjected to a uniform pressure, p. The plate was modeled using the 16-node displacement-based element with the mesh given in Figure 27a. Figures 27b and 27c show results obtained when the normal rotation θ_s is set to zero. We observe that the predicted shearing force is equal to the shearing force calculated by the Kirchhoff plate theory when the twisting moment contribution is neglected. This twisting moment is resisted by the moment reaction M_{ns}, for which the calculated values are close to the Kirchhoff solution. We note that there is no boundary layer in the solution. Also, the corner reaction forces are zero and hence in this physical situation the plate does not have the tendency to rise at the corner.

6. SAMPLE SOLUTIONS AND EVALUATION OF ELEMENTS

The analyses presented in this section have been chosen to illustrate the predictive capabilities of the MITC4, MITC8, MITC9 and MITC16 elements. As previously mentioned, these elements are believed to be very effective general purpose shell elements.

Of course, these elements do not contain any spurious zero energy modes. The analyses were conducted using the ADINA program, version 6.0 [42], modified by the implementation of the MITC9 and MITC16 elements.

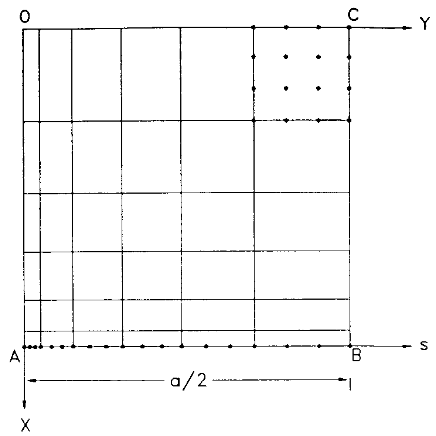

(a) Finite element idealizations using 16-node displacement-based elements

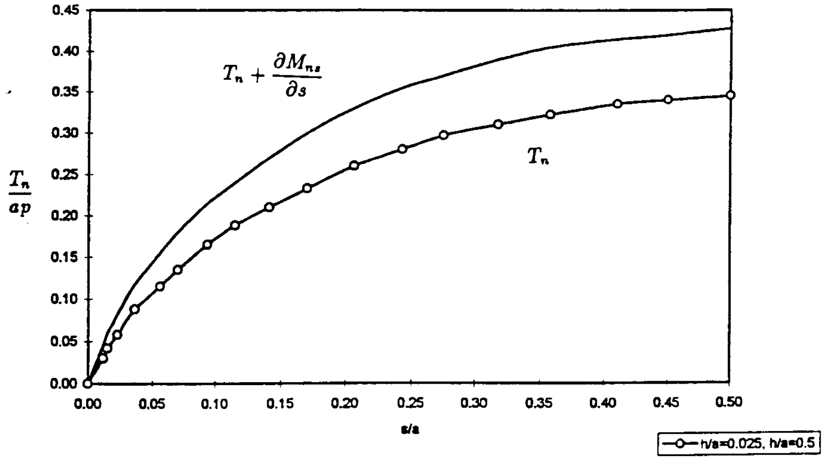

(b) Shearing force distribution along AB assuming $\theta_s = 0$

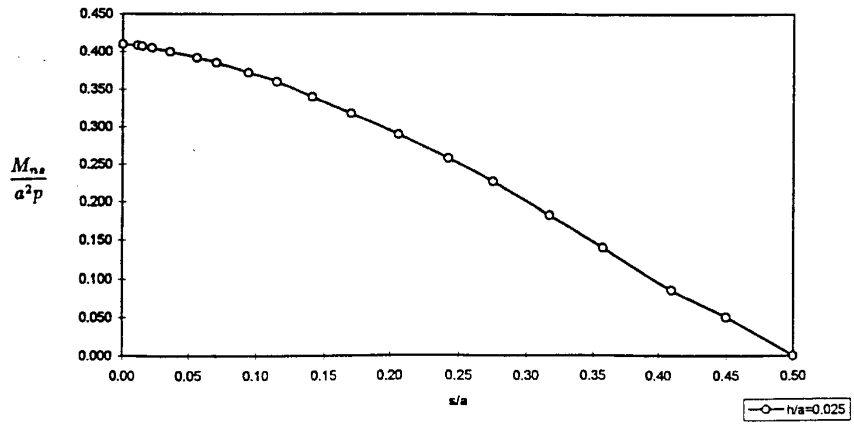

(c) Twisting moment distribution along AB assuming $\theta_s = 0$

Figure 27. Analysis of simply-supported plate. "Hard" boundary conditions

6.1 Patch Test

The patch test has been widely used as a test for element convergence, despite its limitations for mixed formulations. We use the test here to assess the sensitivity of our elements to geometric distortions.

The test we use has been reported earlier (e.g., [21]); namely a patch of elements (with not all of the elements of rectangular shape) is subjected to the minimum displacement/rotation boundary conditions to restrain the structure from rigid body motion. The boundary of the patch is subjected to the tractions that correspond to the constant stress states.

The behavior of the elements is considered satisfactory if the constant stress state is represented by the finite element model.

The above patch test is a standard procedure to test for constant stress states. Of course, we may also test whether higher-order stress variations can be properly represented by the patch. This is achieved by subjecting the patch of elements to the body forces and boundary tractions that correspond (in the plate theory solution) to the stress variations to be predicted by the patch. Then the finite element stress predictions can be compared with the desired higher-order stress variations.

The MITC4, MITC8, MITC9 and MITC16 elements can represent the constant stress states as long as the element sides are straight.

6.2 Analysis of a Clamped Square Plate

Figure 28 shows the square plate considered in this analysis. Note that the thickness to length ratio is 1000. Hence, we consider a thin plate and models with elements that shear lock would give highly inaccurate results.

Figure 28 also shows a typical 2×2 mesh used and in Figure 29 two distorted element mesh layouts are shown. The meshes distort-1 and distort-2 would of course hardly be used in practice, but have merely been selected here to test the predictive capabilities of the elements.

Tables 2 and 3 list the results obtained in the plate analyses using the different elements. The results in particular indicate the high predictive capability of the MITC8 element.

6.3 Analysis of a Skew Plate

The Morley skew plate problem has also been used as a test problem for plate/shell elements. The data of the problem is presented in Figure 30. Generally, the results reported refer to the vertical displacement at the center of the plate *i.e.*, at point E, and these are presented for the MITC plate and shell elements in [38]. Here we show selected results of a modal analysis. In Figures 31 and 32 we show the "Sussman-Bathe" band plots [44] for the vertical displacement component of the eigenvector and for the average in-plane modal stresses at the top surface of the plate. The results are shown for mode 2 and for the MITC4 and MITC8 elements. A uniform mesh of (16×16) MITC4 elements and a uniform mesh of (8×8) MITC8 elements are used. We observe that the displacement results obtained are quite similar for both types of elements. However, the accuracy of the modal stress predictions are quite different for the elements used. Considering the MITC8 element results we can identify clearly continuous stress bands across element boundaries indicating the adequacy of this mesh for these modal stress predictions whereas in the MITC4 element results we cannot identify a distinguishable stress band pattern. These sample results show once more the importance of using higher-order elements when a stress response is sought.

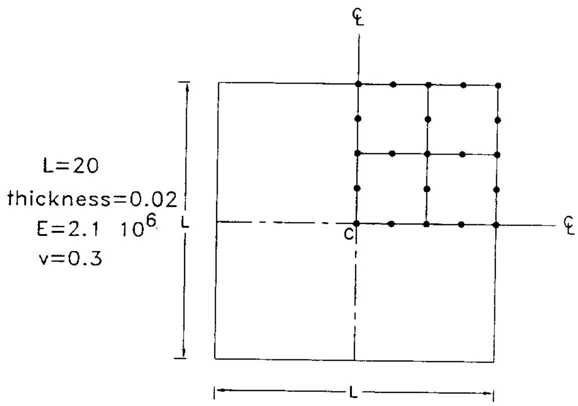

Figure 28. Analysis of a clamped thin square plate. A 2 × 2 mesh model

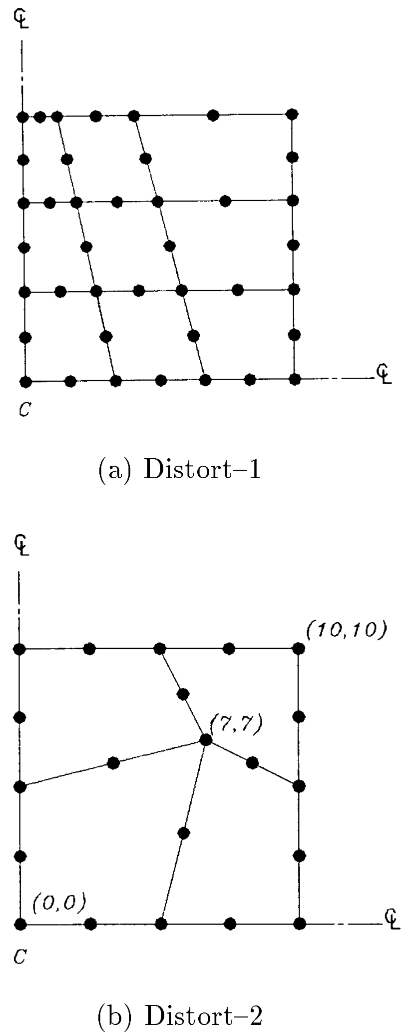

Figure 29. Artificially distorted meshes in the analysis of a clamped plate. One quarter of the mesh shown

Element	Mesh	w_c^{FE}/w_c^{AN} simply-supported	w_c^{FE}/w_c^{AN} clamped
MITC4	1x1	-	-
	2x2	0.9810	0.9631
	3x3	0.9919	0.9852
	distort-1	0.9672	0.8791
	distort-2	0.9807	0.9661
MITC8	1x1	0.9895	1.2401
	2x2	1.0001	1.0060
	3x3	1.0004	1.0050
	distort-1	0.9942	0.9615
	distort-2	1.0006	1.0024
16-node disp.-based element	1x1	1.0155	1.0516
	2x2	1.0013	1.0035
	3x3	1.0009	1.0043
	distort-1	0.9992	0.9600
	distort-2	1.0006	1.0035

Table 2. Performance of the elements in analysis of plate. Uniform pressure loading

Element	Mesh	w_c^{FE}/w_c^{AN} simply-supported	w_c^{FE}/w_c^{AN} clamped
MITC4	1x1	-	-
	2x2	0.9948	0.8666
	3x3	0.9929	0.9390
	distort-1	0.9855	0.8072
	distort-2	0.9843	0.9222
MITC8	1x1	1.0044	1.1161
	2x2	0.9984	1.0005
	3x3	0.9992	1.0007
	distort-1	1.0024	0.9754
	distort-2	0.9986	0.9940
16-node disp. -based element	1x1	0.9550	0.9463
	2x2	0.9890	0.9794
	3x3	0.9952	0.9919
	distort-1	0.9749	0.9176
	distort-2	0.9945	0.9904

Table 3. Performance of the elements in analysis of plate. Concentrated load

6.4 Analysis of a Curve Cantilever

We consider the curved cantilever problem described in Figure 33. In Table 4 we show the results obtained for various meshes using the 16-node displacement-based element and the MITC16 element. The ratio between the finite element and the analytical predictions for the tip rotation, at point A, are shown for several values of thickness. We notice that the predictions are excellent for most discretizations even for extremely thin situations ($h/R = 1/10^5$). However, for the two element model when the side that is common to the

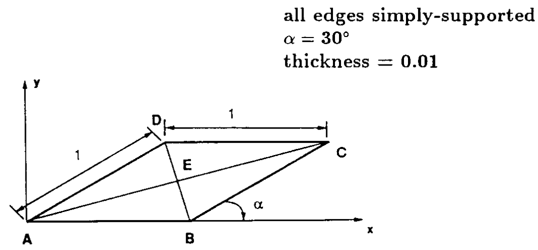

Figure 30. Morley skew plate problem

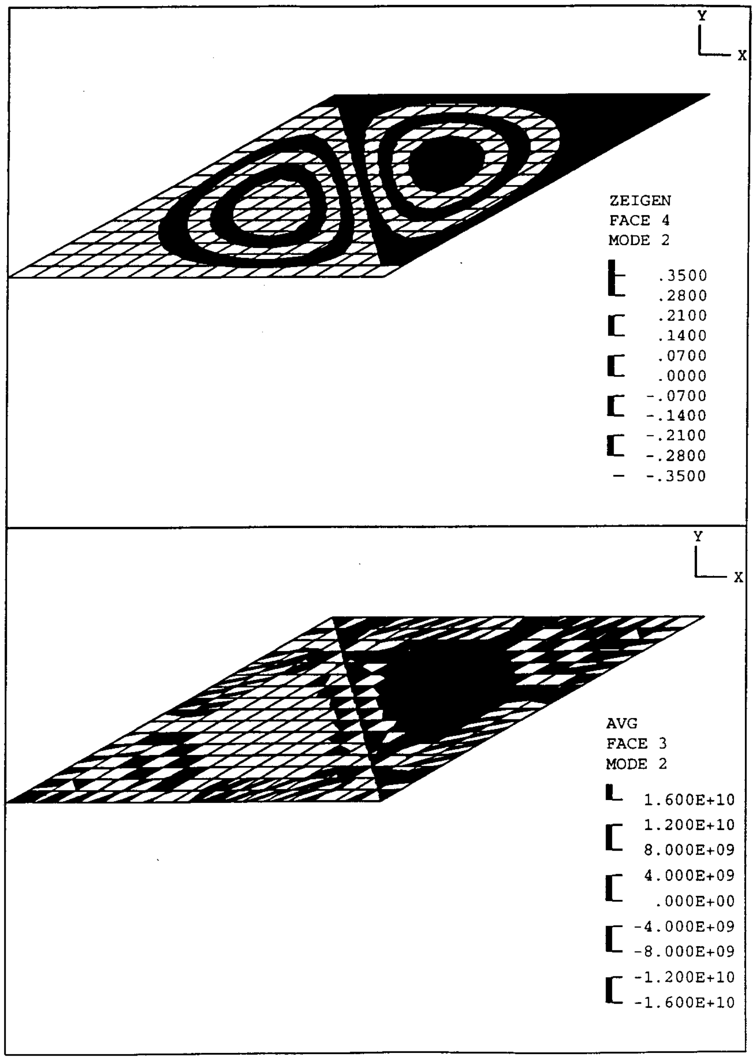

Figure 31. Modal results for the Morley skew plate using a (16 × 16) uniform mesh of MITC4 elements. The symbol AVG stands for the average in plane stress given by $(\sigma_{xx} + \sigma_{yy})/2$ and ZEIGEN for the Z component of the mode eigenvector

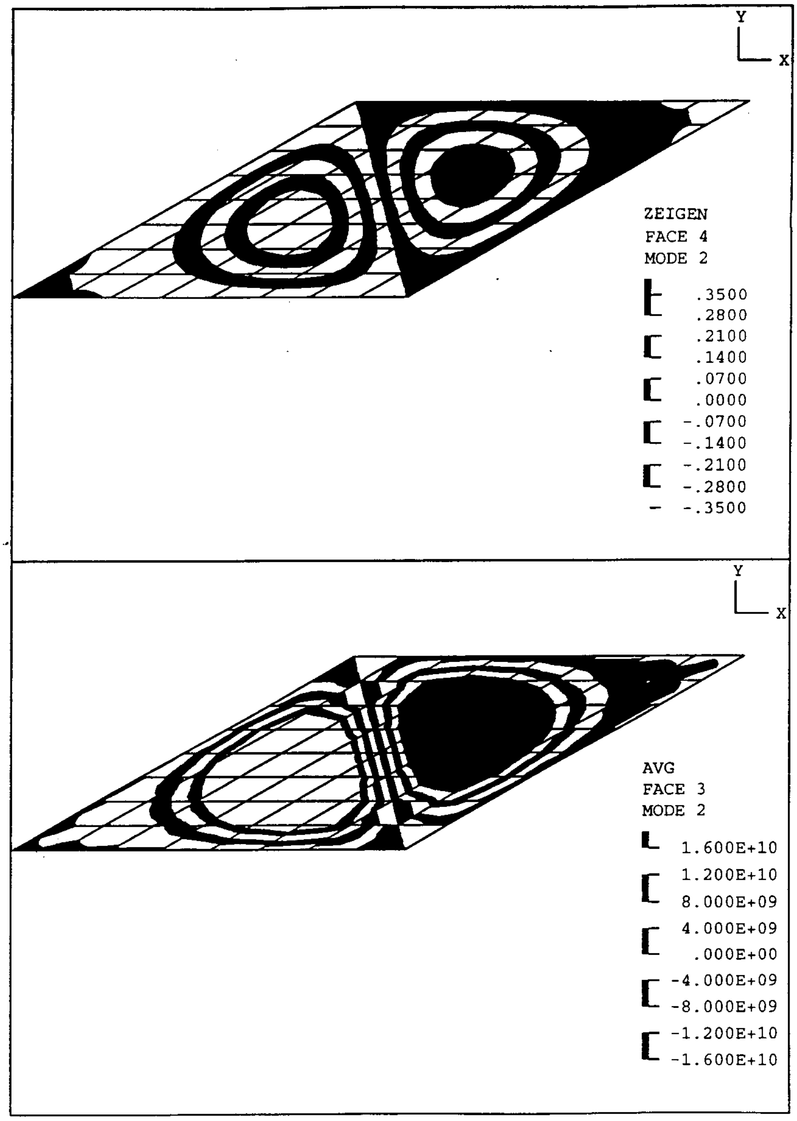

Figure 32. Modal results for the Morley skew plate using a (8×8) uniform mesh of MITC8 elements. The symbol AVG stands for the average in plane stress given by $(\sigma_{xx} + \sigma_{yy})/2$ and ZEIGEN for the Z component of the mode eigenvector

two elements, and is parallel to the axis of the cylindrical surface that describes the curved cantilever, is skewed the results significantly deteriorate for the 16-node displacement-based element displaying a locking behavior. This type of behavior was theoretically predicted by Pitkäranta [26].

In Table 5 we show analogous results for the MITC8 and the MITC9 elements. Using the MITC8 element, which is a good element in general, the results also deteriore significantly for the above case. We notice that the MITC9 element does not display such a behavior.

In the results presented we used $\nu = 0.0$ but the the same kind of solution accuracy is displayed when $\nu = 0.3$.

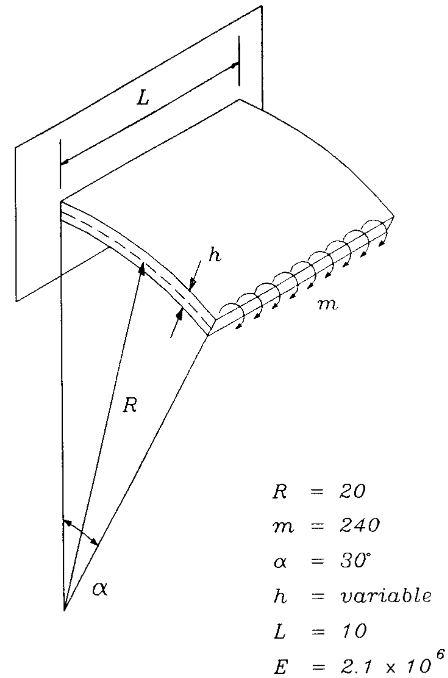

Figure 33. Analysis of a curved cantilever

MESH	h/R	$\theta_{FE} / \theta_{AN}$	
		16 node disp. based	MITC16
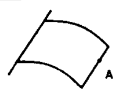	1/100 1/1000 1/100000	0.9995 0.9995 0.9995	1.0001 1.0001 1.0001
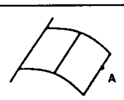	1/100 1/1000 1/100000	0.9996 0.9996 0.9994	1.0000 1.0000 0.9999
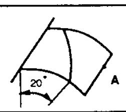	1/100 1/1000 1/100000	0.9868 0.9277 0.0029	0.9975 0.9796 0.9318
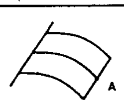	1/100 1/1000 1/100000	0.9995 0.9995 0.9994	1.0001 1.0001 1.0001
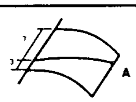	1/100 1/1000 1/100000	0.9993 0.9995 0.9994	1.0000 1.0001 1.0001

Table 4. Summary of results for the curved cantilever problem using 16-node elements. Point A always coincides with an element node

MESH	h/R	$\theta_{FE} / \theta_{AN}$	
		MITC8	MITC9
	1/100 1/1000 1/100000	0.9998 0.9995 0.9995	0.9995 0.9995 0.9995
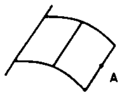	1/100 1/1000 1/100000	1.0001 1.0000 1.0000	1.0000 1.0000 1.0000
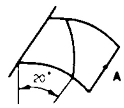	1/100 1/1000 1/100000	0.8958 0.7230 0.0626	0.9956 0.9913 0.9883
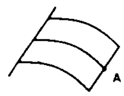	1/100 1/1000 1/100000	0.9996 0.9995 0.9995	0.9995 0.9995 0.9995
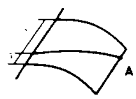	1/100 1/1000 1/100000	0.9999 0.9997 0.9997	0.9995 0.9995 0.9995

Table 5. Summary of results for the curved cantilever problem using 8- and 9-node mixed-interpolated elements. Point A always coincides with an element node

6.5 Analysis of a Pinched Cylinder

The pinched-cylinder problem has been widely used to test shell elements. The physical problem is presented in Figure 34. Due to symmetry conditions only one octant of the cylinder needs to be considered.

Figure 35 shows a typical mesh used in this solution (for 1/8th of the cylinder). This figure also shows that 6 nodal degrees of freedom have been specified at the symmetry lines and otherwise 5 nodal degrees of freedom have been employed. This allocation of nodal point degrees of freedom is efficient because then symmetry conditions can be easily imposed (A similar nodal degree of freedom allocation was used for the analyses discussed below). No attempt was made to identify for the analysis an optimal mesh, but a graded mesh is used because the stresses vary rapidly as the concentrated load is approached.

Table 6 gives the solution results. Note that because of the stress singularity under the concentrated load, this load should be thought of as being distributed over a "small" area if a very fine mesh were to be used [29].

We also performed a study using uniform meshes and the results are shown in Figure 36. The performance of the MITC elements of various orders and also the performance of elements that have been proposed by other authors are shown. In the comparison we used as the index of mesh refinement the number of nodes per side of the region discretized. We notice the excellent performance of the higher–order MITC elements. The results are normalized with respect to the analytical solution for this problem reported by Lindberg *et. al.* [43].

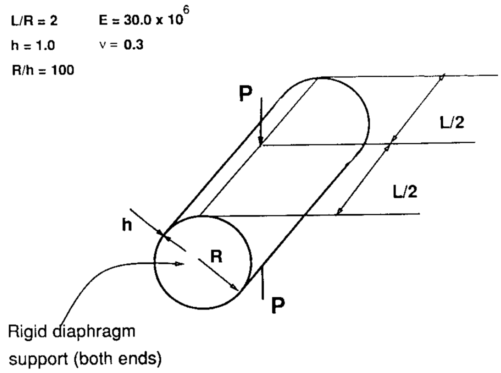

Figure 34. Pinched cylinder problem

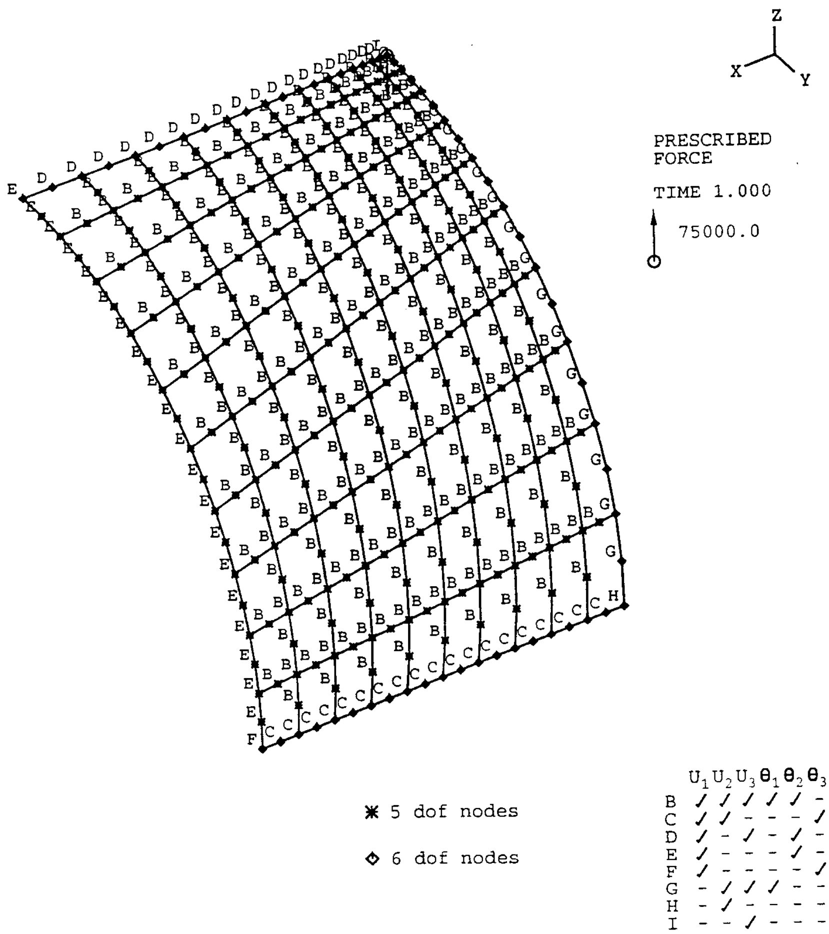

Figure 35. A typical graded mesh used in the analysis of pinched cylinder. One octant of cylinder discretized

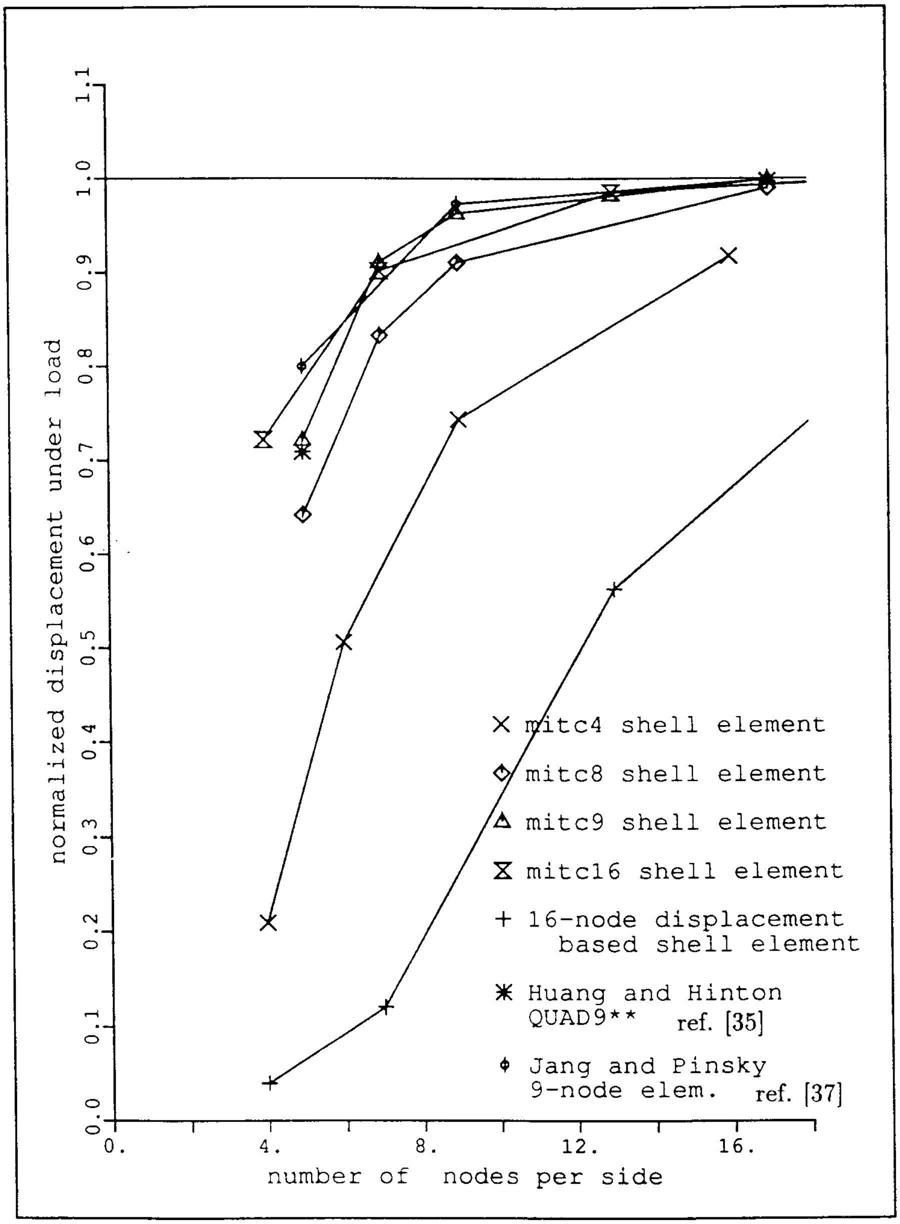

Figure 36. Convergence of various shell elements in pinched cylinder problem using uniform meshes

6.6 Analysis of Scordelis-Lo Shell

This shell problem is also a problem generally considered in the evaluation of shell elements. Figure 37 shows the shell considered and Table 7 lists the solution results obtained.

Element	Mesh	w_c^{FE}/w_c^{AN}	u_D^{FE}/u_D^{AN}
MITC4	5x5	0.4975	0.8725
	8x8	0.7628	0.9609
	10x10	0.8442	0.9733
	15x15	0.9309	0.9883
	20x20	0.9651	0.9937
	30x30	0.9910	0.9979
MITC8	3x3	0.7410	0.8410
	5x5	0.9314	0.9936
	8x8	0.9841	0.9981
	10x10	0.9960	0.9994
	15x15	1.0074	1.0009
16-node disp.-based element	3x3	0.6103	0.8040
	5x5	0.9405	0.9722
	8x8	0.9943	0.9972
	10x10	1.0030	0.9996

Table 6. Performance of elements in analysis of pinched cylinder

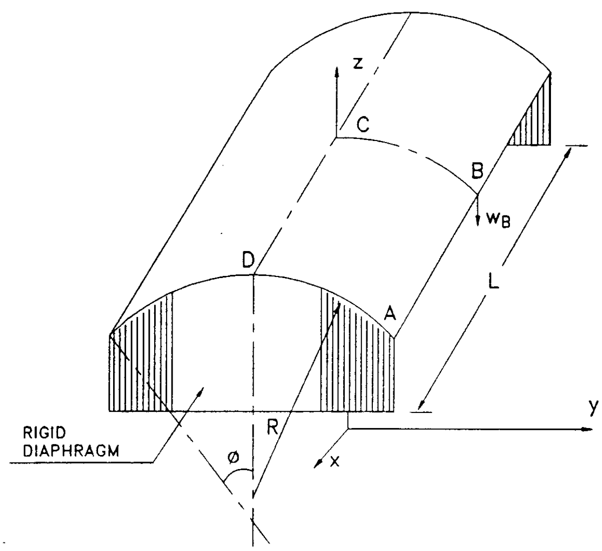

R=300
L=600
Thickness=3.0
E=3.10^6
$\nu = 0.3$
Specific weight = 0.20833
$\phi = 40°$

Figure 37. Scordelis-Lo problem

Element	Mesh	w_B^{FE}/w_B^{AN}
MITC4	2x2	1.1004
	4x4	0.9424
	6x6	0.9733
	10x10	1.0004
MITC8	2x2	0.9347
	4x4	1.0160
	6x6	1.0187
16-node disp.-based element	1x1	0.9987
	4x4	1.0170
	6x6	1.0191

Table 7. Performance of elements in analysis of Scordelis-Lo shell

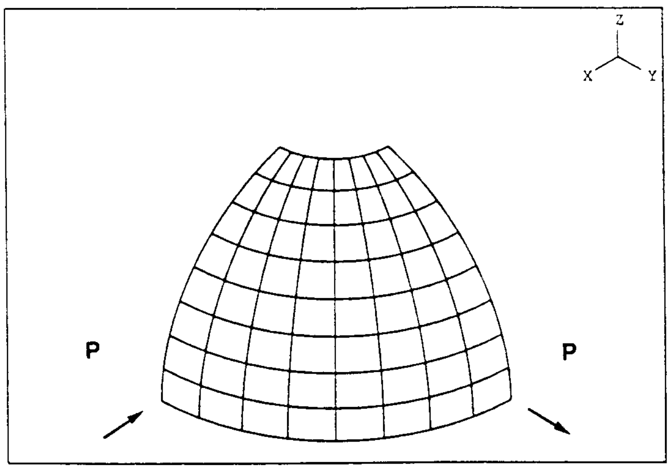

Figure 38. Typical finite element discretization for analysis of hemispherical shell (8×8 mesh). Radius = 10.0, thickness = 0.04, $E = 6.825 \times 10^7$, Poisson's ratio $\nu = 0.3$ and pressure $p = 1.0$

6.7 Analysis of a Hemispherical Shell

The hemispherical shell subjected to self–equilibrating concentrated loads has been used as a benchmark problem for the analysis of doubly curved shells. The hemispherical shell that we analyzed has an 18–degree cut–out on its top and it is free on both bottom and top edges. Only one quarter of the shell needs to be considered and a particular discretization is shown in Figure 38.

The convergence for the displacement under the load is shown in Figure 39 for the cubic elements. The superior performance of the MITC16 element over its displacement-based counterpart is noted. In Figure 40 we show the performance of the MITC9 element compared with the 9-node element proposed by Huang and Hinton [35].

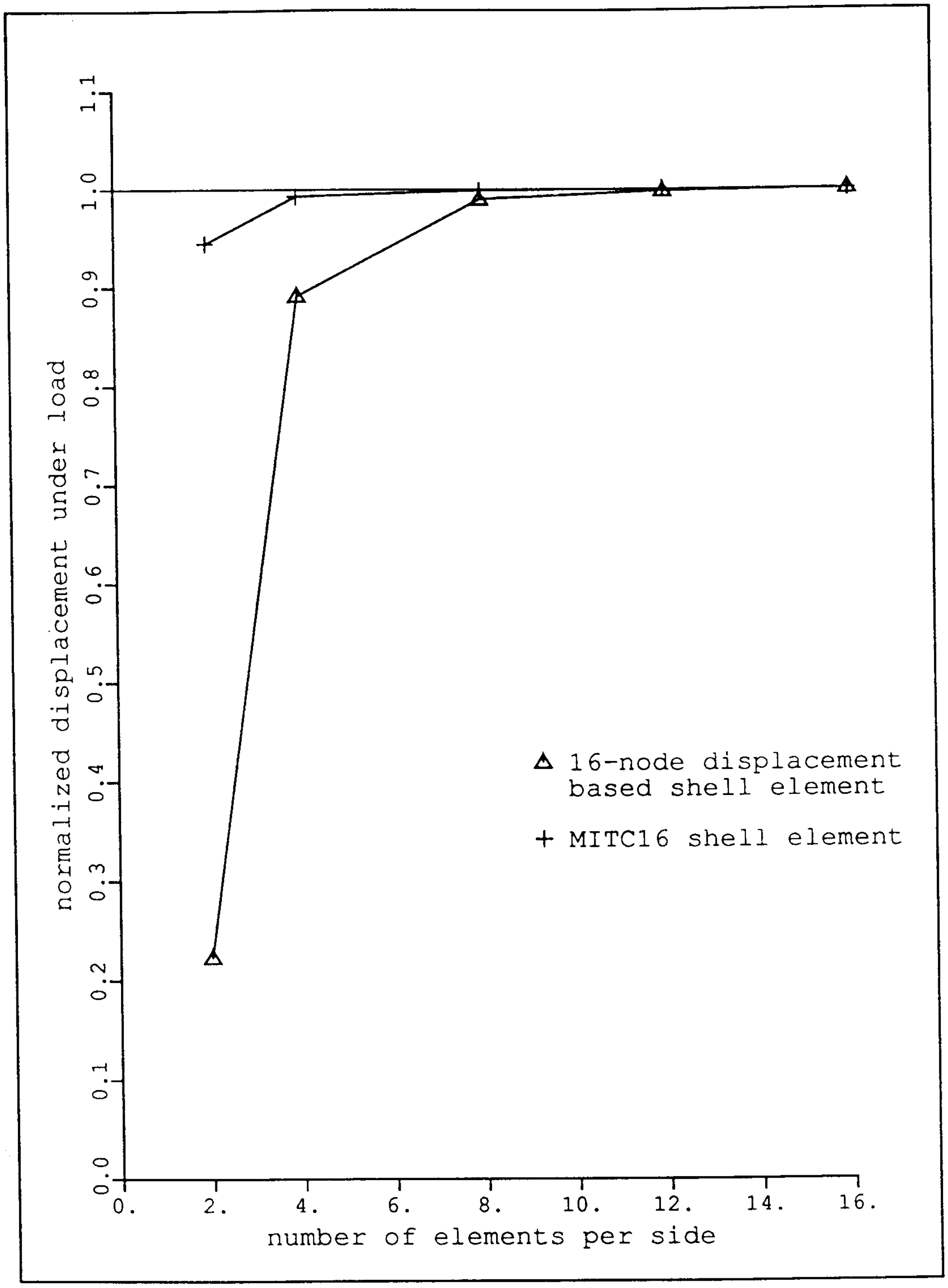

Figure 39. Convergence in analysis of hemispherical shell, cubic elements

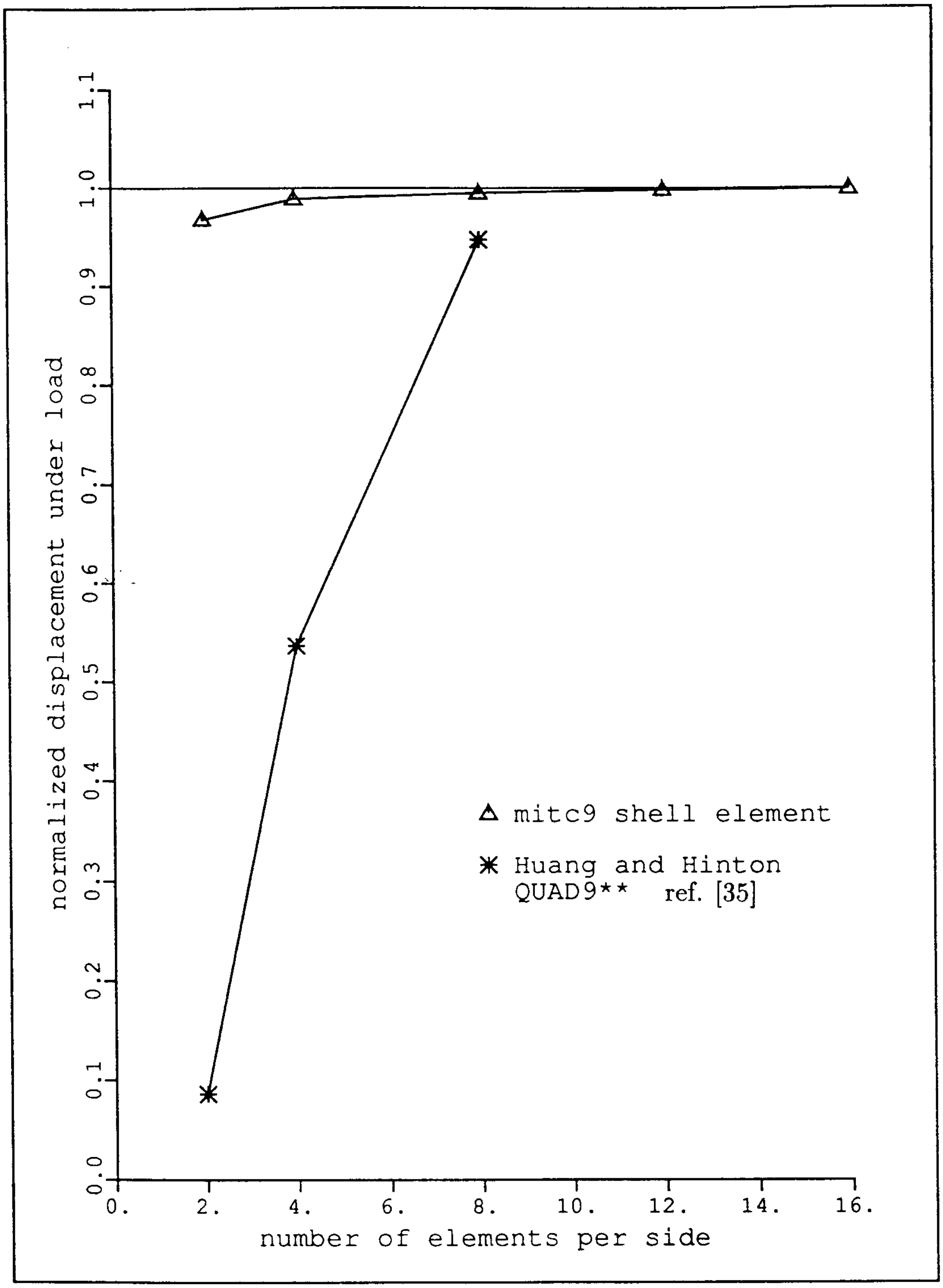

Figure 40. Convergence in analysis of hemispherical shell, 9-node elements

A theoretical lower bound for the displacements under the load was derived by Morley and Morris [45] for the hemispherical shell without the cut–out and it is equal to 0.0924. We used for the normalization of our results the value 0.09355 which corresponds to the converged solution when using the MITC16 element.

6.8 Snap-through of a Shallow Spherical Cap

We analyzed a shallow spherical cap subjected to a concentrated load. The physical model considered is shown in Figure 41. Using a load displacement control method [46] we obtained the complete nonlinear response of the shell including the snap-through response. Due to symmetry conditions only one quarter of the shell needs to be discretized and we used meshes of one and four 16-node elements.

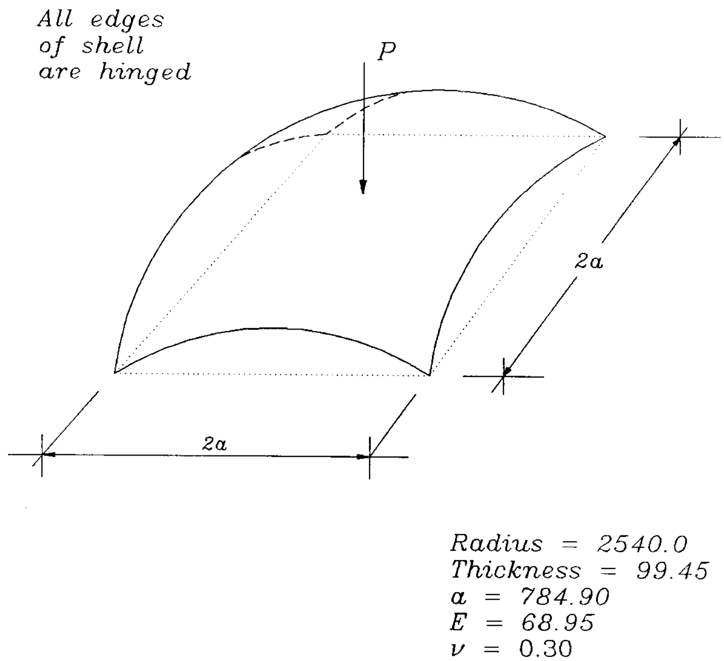

Figure 41. Spherical cap problem

Figures 42 and 43 show the central deflection plotted against the load for the results obtained with the 16-node displacement-based element and the MITC16 element. The solution reported by Leicester [47] using a semi-analytical approach is also shown, just as an additional solution, since it has approximations of its own and should not be regarded as the solution of the mathematical model of the problem in consideration.

We note that the solutions obtained with the MITC16 element using the one and four element meshes are quite close to each other in contrast to the solutions obtained with the 16-node displacement-based element (Figure 42). We also note that the 16-node displacement-based solution with four elements is close to the solutions obtained with the MITC16 element. Hence, we can conclude that for the 16-node displacement-based element at least a four element mesh is required whereas with the MITC16 element a good response prediction is already obtained with only one element for a quarter of the structure.

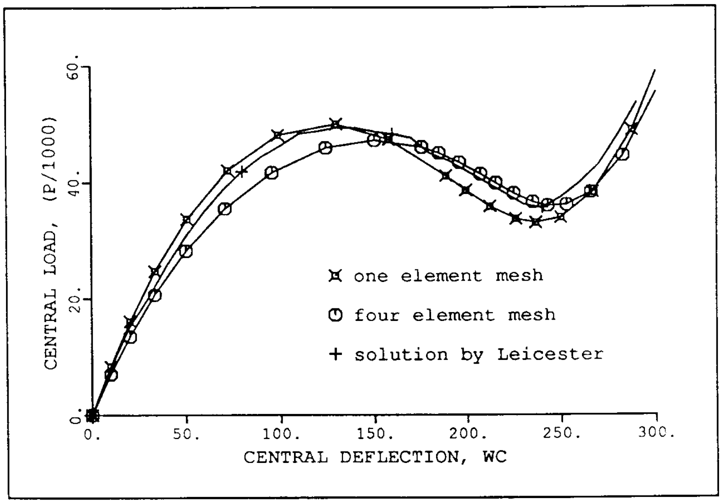

Figure 42. Nonlinear response of a shallow spherical cap subjected to concentrated load using the 16-node displacement based element

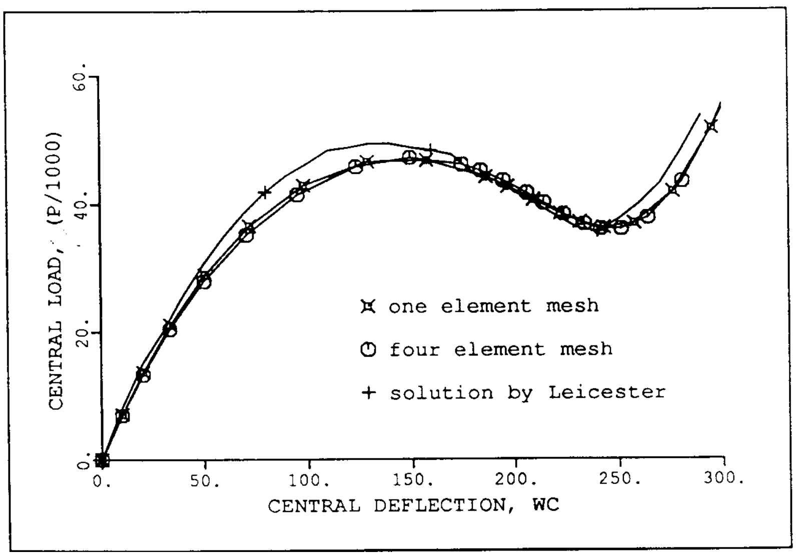

Figure 43. Nonlinear response of a shallow spherical cap subjected to concentrated load using the MITC16 element

6.9 Large Displacement Solution of a Cylindrical Shell

The cylindrical shell shown in Figure 44 was analyzed using three meshes for one quarter of the shell: a 6×6 mesh of MITC4 elements, a 3×3 mesh of MITC8 elements and a 2×2 mesh of 16-node displacement-based elements. In essence identical response solutions were obtained. Figure 45 shows the finite element response of the shell which is very close to the solution reported by Sabir and Lock [48]. In the ADINA solution the load displacement control method was used [29].

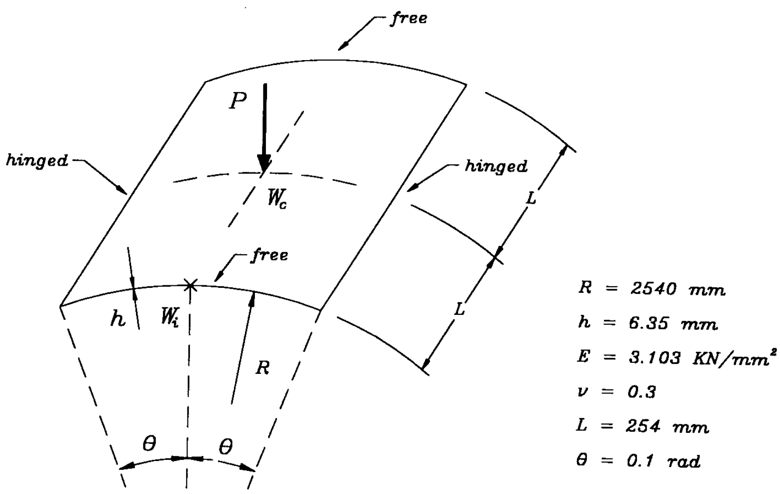

Figure 44. Large displacement analysis of shallow cylindrical shell

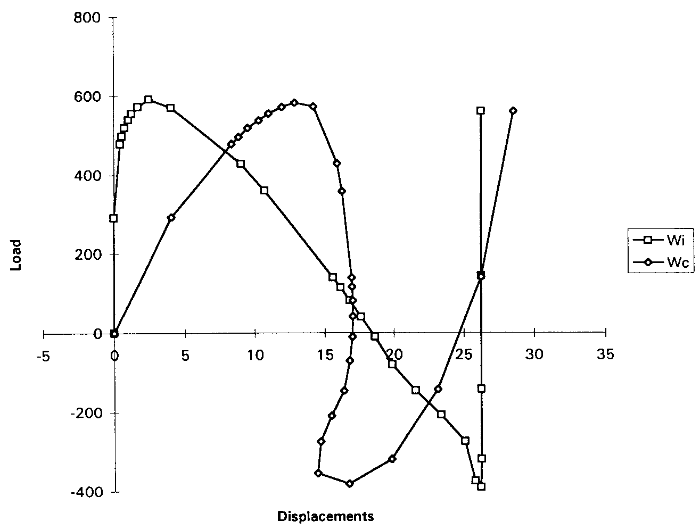

Figure 45. Finite element displacement solutions in analysis of cylindrical shell

7. CONCLUDING REMARKS

The objective in this paper was to summarize some state-of-the-art capabilities for shell structural analysis. The formulation of recommended shell elements and numerical experiences were presented.

The shell analysis capabilities currently available are general and effective and general problems can be solved with confidence. As for future developments, the use of the mixed interpolation for element formulations has significant further potential and is expected to yield additional valuable elements.

REFERENCES

1 Noor, A. *et al.* (eds.) (1989), "Analytical and Computational Models of Shells", *ASME Special Publication*, CED–3.

2 Bathe, K.J. and Dvorkin, E. (1986), "A Formulation of General Shell Elements — the Use of Mixed Interpolation of Tensorial Components", *International Journal for Numerical Methods in Engineering*, **22**, pp. 697–722.

3 Love, A.E.H. (1888), "The Small Free Vibrations and Deformation of a Thin Elastic Shells", *Phil. Trans. Roy. Soc. London*, (Ser. A 179), pp. 491–546.

4 Koiter, W.T. (1959), "A Consistent First Approximation in General Theory of Thin Elastic Shells", In *Proc. IUTAM Symposium on the Theory of Thin Elastic Shells*, Delft, pp. 12–33.

5 Sanders, J.L. Jr. (1959), "An Improved First Approximation Theory for Thin Shells", *Tech. Report R-24*, NASA.

6 Kardestuncer, H. (ed.) (1987), "*Finite Element Handbook*", MacGraw-Hill.

7 Ahmad, S., Irons, B.M. and Zienkiewicz, O.C. (1970), "Analysis of Thick and Thin Shell Structures by Curved Finite Elements", *International Journal for Numerical Methods in Engineering*, **2**, pp. 419–451.

8 Ramm. E. (1977), "A Plate/Shell Element for Large Deflections and Rotations", In Bathe, K.J. (ed.), *Formulations and Computational Algorithms in Finite Element Analysis*, M.I.T. Press.

9 Bathe, K.J. and Bolourchi, S. (1979), "A Geometric and Material Nonlinear Plate and Shell Element", *Computers & Structures*, **11**, 23–48.

10 Zienkiewicz, O.C., Taylor, R.L. and Too, J.M. (1971), "Reduced Integration Techniques in General Analysis of Plates and Shells", *International Journal for Numerical Methods in Engineering*, **3**, pp. 275–290.

11 Oñate, E., Hinton, E. and Glover, N. (1978), "Techniques for Improving the Performance of the Ahmad Shell Elements", *Proc. Int. Conf. on Applied Numerical Modelling*, Pentech Press, Madrid, pp. 30–53.

12 Hughes, T.J.R., Cohen, M. and Haroun, M. (1978), "Reduced and Selective Integration Techniques in the Finite Element Analysis of Plates", *Nuclear Engineering Design*, **46**, pp. 203–222.

13 Malkus, D.S. and Hughes, T.J.R. (1978), " Mixed Finite Element Methods-Reduced and Selective Integration Techniques: A Unification of Concepts", *Computer Methods in Applied Mechanics and Engineering*, **15**, pp. 63–81.

14 Bercovier, M. (1978), "Perturbation of a Mixed Variational Problems, Applications to Mixed Finite Element Methods", *R.A.I.R.O. Anal. Numer.*, **12**, pp. 211–236.

15 Belytschko, T., Liu, W.K., Ong, S.J. and Lam, D. (1985), "Implementation and Application of a 9-node Lagrange Shell Element with Spurious Mode Control", *Computers & Structures*, **20**, (1-3), pp. 121–128.

16 Belytschko, T., Ong, S.J. and Liu, W.K. (1985), "A Consistent Control of Spurious Singular Modes in the 9–Node Lagrangian Element for the Laplace and Mindlin Plate Equations" *Computer Methods in Applied Mechanics and Engineering*, **44**, pp. 269–295.

17 Bathe, K.J. and Brezzi, F. (1985), "On the Convergence of a Four-Node Plate Bending Element Based on Mindlin/Reissner Plate Theory and a Mixed Interpolation", In Whiteman, J.R. (ed.), *Proceedings of the Conference on Mathematics of Finite Elements and Applications V*, Academic Press, pp. 491–503.

18 Bathe, K.J. and Brezzi, F. (1987), "A Simplified Analysis of Two–Plate Bending Elements – the MITC4 and MITC9 Elements", In Pande, G.N. and Middleton, J. (eds.), *Proceedings of the International Conference on Numerical Methods in Engineering (NUMETA 87)*, University College of Swansea, Wales, p. D46.

19 Brezzi, F., Bathe, K.J. and Fortin, M. (1989), "Mixed-Interpolated Elements for Reissner-Mindlin Plates", *International Journal for Numerical Methods in Engineering*, **28**, pp. 1787–1801.

20 Brezzi, F., Fortin, M. and Stenberg, R. (1991), "Error Analysis of Mixed–Interpolated Elements for Reissner–Mindlin Plates", *Mathematical Models and Methods in Applied Sciences*, **1**, pp. 125–151.

21 Dvorkin, E. and Bathe, K.J. (1984), "A Continuum Mechanics Based Four-Node Shell Element for General Nonlinear Analysis", *Engineering Computations*, **1**, pp. 77–88.

22 Bathe, K.J. and Dvorkin, E. (1985), "A Four-Node Plate Bending Element Based on Mindlin–Reissner Plate Theory and a Mixed Interpolation", *International Journal for Numerical Methods in Engineering*, **21**, pp. 367–383.

23 Bathe, K.J., Cho, S.W., Bucalem, M.L. and Brezzi, F. (1989), "On Our MITC Plate Bending/Shell Elements", In Noor, A. *et al.* (eds.), *Analytical and Computational Models of Shells*, CED–3, ASME Special Publication, pp. 261–278.

24 Bathe, K.J., Brezzi, F. and Cho, S.W. (1989), "The MITC7 and MITC9 Plate Bending Elements", *Computers & Structures*, **32**, (3/4), pp. 797–814.

25 Bathe, K.J., Bucalem, M.L. and Brezzi, F. (1990), "Displacement and Stress Convergence of Our MITC Plate Bending Elements", *Engineering Computations*, **7**, 4, pp. 291–302.

26 Pitkäranta, J. (1991), "The Problem of Membrane Locking in Finite Element Analysis of Cylindrical Shells", Report, Helsinki University of Technology, Otakaari 1, SF-02150 Espoo, Finland.

27 Hughes, T.J.R. and Tezduyar, T.E. (1981), "Finite Elements Based upon Mindlin Plate Theory with Particular Reference to the Four-Node Bilinear Isoparametric Element", *Journal of Applied Mechanics, Transactions of ASME*, **48**, pp. 587–596.

28 MacNeal, R.H., (1982), "Derivation of Element Stiffness Matrices by Assumed Strain Distributions", *Nuclear Engineering Design*, **70**, pp. 3–12.

29 Bathe, K.J. (1996), "*Finite Element Procedures*", Prentice Hall, Inc., Englewood Cliffs.

30 Schweizerhof, K. and Ramm, E. (1984), "Displacement Dependent Pressure Loads in Nonlinear Finite Element Analysis", *Computers & Structures*, **28**, pp. 1099-1114.

31 Argyris, J. (1982), "An Excursion with Large Rotations", *Computer Methods in Applied Mechanics and Engineering*, **32**, pp. 85-155.

32 Bathe, K.J. (1986), "Finite Elements in CAD and ADINA", *Journal of Nuclear Engineering and Design*, **98**, pp. 57–67.

33 Bathe, K.J. and Ho, L. (1981), "Finite Elements in CAD and ADINA", *Nonlinear Finite Element Analysis in Structural Mechanics*, Wunderlich, W. *et al.* (eds.), Springer Verlag, Berlin.

34 Hughes, T.J.R., Taylor, R.L. and Kanoknukulchai (1977), "A Simple and Efficient Finite Element for Plate Bending", *International Journal for Numerical Methods in Engineering*, **11**, pp. 1529-1543.

35 Huang, H.C. and Hinton, E. (1986), "A New Nine–Node Degenerated Shell Element with Enhanced Membrane and Shear Interpolation", *International Journal for Numerical Methods in Engineering*, **22**, pp. 73–92.

36 Park, K.C. and Stanley, G.M. (1986), "A curved C^0 Shell Element Based on Assumed Natural-Coordinate Strains", *Journal of Applied Mechanics, Transactions of ASME*, *53*, pp. 278–290.

37 Jang, J. and Pinsky, P.M. (1987), "An Assumed Covariant Strain Based 9-Node Shell Element", *International Journal for Numerical Methods in Engineering*, **24**, pp. 2389–2411.

38 Bucalem, M.L. and Bathe, K.J. (1993), "Higher-Order MITC General Shell Elements", *International Journal for Numerical Methods in Engineering*, **36**, pp. 3729–3754.

39 Sussman, T. and Bathe, K.J. (1987), "A Finite Element Formulation for Nonlinear Incompressible Elastic and Inelastic Analysis", *Computers & Structures*, **26**, pp. 357–409.

40 Häggblad, B. and Bathe, K.J. (1990), "Specifications of Boundary Conditions for Reissner–Mindlin Plate Bending Finite Elements", *International Journal for Numerical Methods in Engineering*, **30**, pp. 981–1011.

41 Arnold, D.N. and Falk, R.S. (1989), "Edge Effects in Reissner–Mindlin Plate Theory", In Noor, A. *et al.*, (eds.) *Analytical and Computational Models of Shells*, CED–3, ASME Special Publication.

42 ADINA R&D (1990), "ADINA–A Finite Element Program for Automatic Dynamic Incremental Nonlinear Analysis", Report 90–1, ADINA R&D, Watertown, MA.

43 Lindberg, G.M., Olson, M.D. and Cowper, E.R. (1969), "New Developments in the Finite Element Analysis of Shells", *National Research Council of Canada, Quarterly Bulletin of the Division of Mechanical Engineering and the National Aeronautical Establishment*, **4**, pp. 1–38.

44 Sussman, T. and Bathe, K.J. (1986), "Studies of Finite Element Procedures. Stress Band Plots and the Evaluation of Finite Element Meshes", *Engineering Computations*, **3**, pp. 178–191.

45 Morley, L.S.D. and Morris, A.J. (1978), "Conflict Between Finite Elements and Shell Theory", Technical report, Royal Aicraft Establishment Report, London.

46 Bathe, K.J. and Dvorkin, E.N. (1983), "On the Automatic Solution of Nonlinear Finite Element Equations", *Computers & Structures*, **17**, 5-6, pp. 871–879.

47 Leicester, R.H. (1968), "Finite Deformations of Shallow Shells", In *Proceedings of American Society of Civil Engineers*, **94**, (EM6), pp. 1409–1423.

48 Sabir, A.B. and Lock, A.C. (1973), "The Application of Finite Elements in the Large Deflection Geometrically Nonlinear Behavior of Cylindrical Shells", In Brebbia, A. and Totteham, H. (eds.), *Variational Methods in Engineering*, pp. 7/66–67/75, Southampton University Press.

49 Chapelle, D. and Bathe, K.J. (1993), "The Inf-Sup Test", *Computer and Structures*, **47**, pp. 537–545.

Please address your comments or questions on this paper to:
International Center for Numerical Methods in Engineering
Edificio C-1, Campus Norte UPC
Gran Capitán s/n
08034 Barcelona, Spain
Phone: 34-3-4016035; Fax: 34-3-4016517